Controlled Microfluidic Synthesis of Biological Stimuli-Responsive Polymer Nanoparticles

Yuhang Huang, Arman Moini Jazani, Elliot P. Howell, Jung Kwon Oh, & Matthew G. Moffitt

December 2019

Citation for this paper:

Huang, Y., Jazani, A. M., Howell, E. P., Oh, J. K., & Moffitt, M. G. (2019). Controlled Microfluidic Synthesis of Biological Stimuli-Responsive Polymer Nanoparticles. *ACS Applied Materials & Interfaces*, 12(1), 177-190. https://doi.org/10.1021/acsami.9b17101.

Controlled Microfluidic Synthesis of Biological Stimuli-Responsive Polymer Nanoparticles

Yuhang Huang, Arman Moini Jazani,[¥] *Elliot P. Howell, Jung Kwon Oh,*[¥] *and Matthew G. Moffitt**

Department of Chemistry, University of Victoria, PO Box 1700 Stn CSC, Victoria, BC V8W 2Y2 Canada

[¥]Department of Chemistry and Biochemistry, Concordia University, 7141 Sherbrooke St. West, Montreal, Quebec H4B 1R6, Canada

ABSTRACT

Microfluidic flow-directed self-assembly of biological stimuli-responsive block copolymers is demonstrated with dual-location cleavable linkages at the junction between hydrophilic and hydrophobic blocks and on pendant groups within the hydrophobic blocks. On-chip self-assembly within a two-phase microfluidic reactor forms various "DualM" polymer nanoparticles (PNPs), including cylinders and multi-compartment vesicles, with sizes and morphologies that are tunable with manufacturing flow rate. Complex kinetically-trapped intermediates between shear-dependent states provide the most detailed mechanism to date of microfluidic PNP formation in the presence of flow-variable high shear. Glutathione (GSH)-triggered changes in PNP size and internal structure depend strongly on the initial flow-directed size and internal structure. Upon incubation in GSH, flow-directed PNPs with smaller average sizes showed faster hydrodynamic size increase (attributed to junction cleavage) and those with higher excess Gibbs free energy showed faster inner compartment growth (attributed to pendant cleavage). These results demonstrate that the combination of chemical control of the location of biologically-responsive linkages with microfluidic shear processing offers promising routes for tunable “smart” polymeric nanomedicines.

KEYWORDS: stimuli-responsive block copolymers, nanoparticles, microfluidics, directed self-assembly, drug delivery

INTRODUCTION

Amphiphilic block copolymers self-assemble in aqueous media to form polymer nanoparticles (PNPs) of variable morphologies that are promising nanocarriers for drug delivery.[1-16] Drug delivery PNPs encapsulate hydrophobic drugs within the hydrophobic cores surrounded by hydrophilic coronal chains, increasing bioavailability[6,8] and size selectivity (EPR effect)[2,12,14,15] of the drug. However, a central challenge in the design of PNP-based drug delivery vehicles is presence of uncontrolled drug release outside of the target region.[17-19] For chemotherapeutics in particular, it is important to enhance release in the tumor in order to increase efficacy and minimize side effects within healthy tissue. Block copolymers that dissociate in response to external stimuli, including temperature,[20-22] light,[23-26] and pH,[27-32] provide the potential for "smart" enhanced release in cancerous tumor microenvironments.[33,34]

Overexpressed reduction-oxidation reactions within cancer cells have recently been explored as potential triggers for stimuli-responsive block copolymers.[35-37] For example, glutathione (GSH) is a tripeptide-containing cysteine with a pendant thiol (-SH) group which acts as a cellular reducing agent. GSH is found at different concentrations in intracellular and extracellular regions of healthy tissue and at highly elevated concentrations (>10 mM) within cancer cells,[38,39] providing a chemical stimulus for specially-designed block copolymers. Specifically, disulfide linkages introduced into the structure of a block copolymer can be cleaved to the corresponding thiols in the presence of GSH or other reducing agents.[40-50] These disulfide linkages can be located at the junction of hydrophilic and hydrophobic blocks (junction linkages), producing PNPs with GSH-cleavable coronal chains. [40-42, 44-47] Alternatively, the disulfide linkages can be introduced at the junction of pendant chains within the hydrophobic block (pendant linkages), leading to GSH-induced destabilization of the PNP hydrophobic cores and a dramatic increase in release rate of the drug.[43,48,49]

Recently, dual GSH-responsive block copolymers with disulfide linkages in *both* junction *and* pendant locations were synthesized and used to prepare "DualM" PNPs for drug delivery.[50] The block copolymer consists of a hydrophilic poly(ethylene oxide) (PEO) block and a hydrophobic polymethacrylate block having disulfide pendants (PHMssEt), with a disulfide junction between the hydrophobic and hydrophilic blocks (PEO-ss-PHMssEt). PNPs showed controlled drug release inside HeLa cells with 10 mM GSH due to the cleavage of disulfides at both locations within the reductive cellular environment. The results demonstrate the potential for synergistically-enhanced drug release enabled by dual locations of stimuli-responsive cleavable linkages.

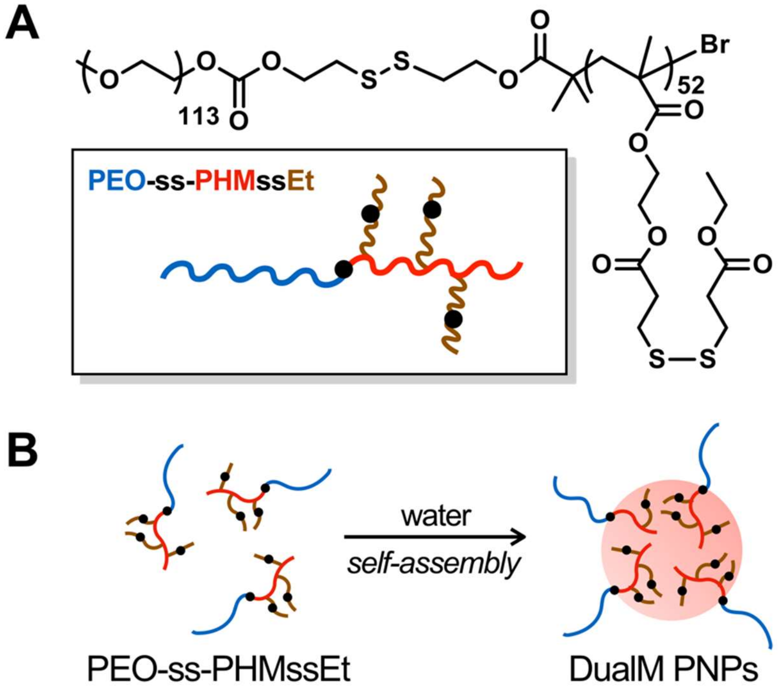

Figure 1. (A) Molecular structure of PEO-ss-PHMssEt copolymers. (B) Schematic of DualM PNP formation through self-assembly in aqueous solution.

Current approaches to controlling the responsivity of stimuli-responsive PNPs are chemical in nature, involving the design and synthesis of new copolymers with cleavable groups of variable composition, number, and location within the copolymer molecule.[42,43,47,51] Microfluidic approaches offer new routes to the synthesis of nanomedicines with high throughput and improved control.[11,52-54] In our group, we have shown that variable flow-directed shear forces within high-shear "hot spots" of two-phase segmented microfluidic reactors provides processing control over self-assembly, leading to PNPs with controllable structure and properties[55-67], including drug encapsulation efficiencies,[57,59,62-67] release rates,[57,59,62-67] and *in vitro* cytotoxicity.[63-67] In addition, we recently showed that microfluidic self-assembly of photoresponsive poly(*o*-nitrobenzyl acrylate)-*block*-polydimethylacrylamide (PNBA-*b*-PDMA) block copolymers provides processing control of photo-triggered dissociation rates of the resulting PNPs.[60]

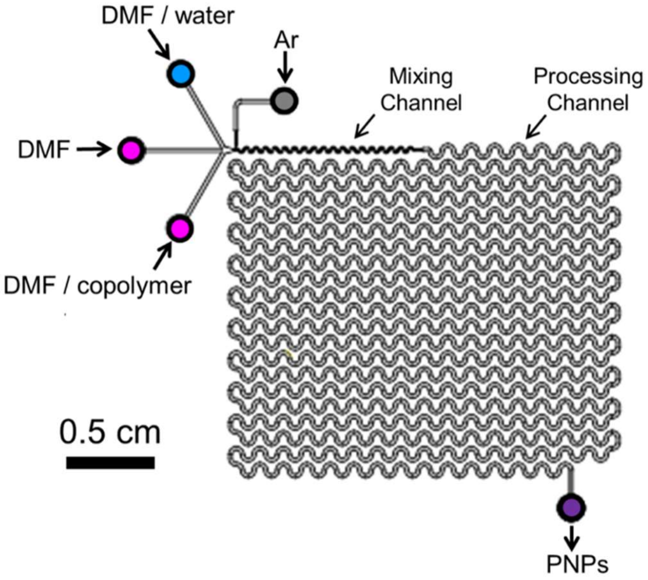

Figure 2. Schematic of the two-phase gas-liquid segmented microfluidic reactor.

In this study, we demonstrate the preparation and characterization of DualM GSH-responsive PNPs from a PEO-ss-PHMssEt block copolymer (Figure 1) in a two-phase microfluidic reactor at various flow rates. We show that tunable shear forces within the microchannels provide control over the size distributions, morphologies, internal structure, and GSH responsivities of the PNPs. Mainly spherical solid PNPs with broad size dispersity are formed by conventional bulk nanoprecipitation, whereas microfluidic PNP formation yields intriguing flow-dependent morphologies, including spheres, cylinders, vesicles, and complex multi-compartment vesicles with internal symmetry. Previous work from our group has demonstrated microfluidic morphological control of block copolymer PNPs, although the detailed mechanisms of on-chip morphology formation were not elucidated in those systems. However, we find that microfluidic assembly of DualM copolymer gives rise to complex and intriguing kinetically-trapped intermediates between shear-dependent states, providing the most detailed mechanism to date of microfluidic PNP formation in the presence of flow-variable high shear. Moreover, we find distinct differences in GSH-triggered responsivities for PNPs formed under different conditions of microfluidic flow, pointing to combined roles of linkage location and shear processing in controlling the rates of both particle and inner compartment growth upon GSH exposure. These results show that new routes to finely-tuned smart nanomedicines can be achieved by combining bottom-up chemical design of stimuli-responsive polymer materials with top-down mechanical processing in microfluidic channels.

EXPERIMENTAL SECTION

Materials. Copper(II) bromide ($CuBr_2$, >99.99%), anisole (anhydrous, >99%), tin(II) 2-ethylhexanoate ($Sn(EH)_2$, 95%), and L-glutathione (GSH, >98%) purchased from Sigma-Aldrich, *N*,*N*-dimethylformamide (DMF, >99.9%) from Fisher Scientific was used as received without further purification. Tris(2-pyridylmethyl)amine (TPMA),[68] a poly(ethylene glycol)-based bromine labeled with a disulfide linkages (PEO-ss-Br),[47] and a methacrylate bearing a pendant disulfide linkage (HMssEt)[69] were synthesized according to literature procedures.

Synthesis of GSH-Responsive PEO-ss-PHMssEt Block Copolymer. The synthesis of GSH-responsive PEO-ss-PHMssEt block copolymer is described previously.[50] Briefly, atom transfer radical polymerization was conducted for HMssEt mediated with $CuBr_2$/TPMA complex in the presence of PEO-ss-Br macroinitiator in anisole at 40 °C. $Sn(EH)_2$ was used to reduce Cu(II) species to active Cu(I) species to initiate the polymerization. The formed copolymer was purified by passing through a basic alumina column to remove residual copper and following precipitation from hexane.

After purification, the resulting block copolymer was characterized by gel permeation chromatography (GPC, Figure S1) and found to have a number-average molecular weight of M_n = 29 000 g/mol and a dispersity of $Đ$ = 1.12. Proton nuclear magnetic resonance (^{1}H NMR, Figure S2) was used to determine the degree of polymerization (DP) of the PHMssEt block, which was found to be 52 by comparing proton integrations from the PEO (previously known DP = 113) and PHMssEt blocks, as described previously.[50]

Critical Water Content (cwc) Determination. The cwc is the minimum water content that is required for block copolymer self-assembly into micellar aggregates. Static light scattering (SLS) measurements were carried out to determine the cwc of 0.33 wt % copolymer in DMF solution, which was the initial condition for all self-assembly experiments in this study. SLS experiments were performed on a Brookhaven Instruments photo-correlation spectrometer equipped with a BI-200SM goniometer, a BI-9000AT digital autocorrelator, and a BI-Mini-L30 30 mW red (636 nm) compact diode laser, at a scattering angle of 90° and a temperature of 25 °C.

Briefly, 1 wt % copolymer stock solution in DMF was prepared and stirred overnight. This solution was filtered through 2 × 0.45 μm nominal pore size Teflon syringe filters (VWR) into pre-cleaned scintillation vials, and then was diluted to a final concentration of 0.33 wt % by gravimetric addition of DMF. To the resulting ~5 g of solution, deionized water was added in successive 0.03−0.06 g quantities using a microsyringe equipped with 2 × 0.20 μm nominal pore size nylon syringe filters (National Scientific). After each addition of water the sample was allowed to equilibrate for 15 min before the scattered light intensity was measured. The resulting scattered light intensity was plotted vs. water concentration. Then the cwc value was determined from the intercept of linear fits to the baseline and the sharply-increasing intensity region. A representative titration plot and cwc determination for the copolymer is shown in Figure S3. Determinations of cwc were carried out in triplicate from the same stock solution and the mean value and standard error of the three measurements were used to calculate the reported cwc and experimental error of 11.7 ± 0.2 wt %.

Bulk Preparation of DualM PNPs. The DualM PNPs were firstly prepared by the conventional bulk method of nanoprecipitation. Specifically, ~1 g of 0.33 wt % copolymer stock solution in DMF was prepared and stirred overnight to equilibrate. The resulting 1 mL of solution was then added at a constant injection rate of 120 μL/min using a syringe pump into a 10× excess volume of deionized water with vigorous stirring. In order to remove residual DMF, the resulting PNP dispersions were immediately transferred to a 6−8 kDa MWCO dialysis membrane (Spectrum Laboratories) and dialyzed against deionized water for at least 18 h, changing the deionized water every hour for the first 4 h. Although remaining DMF concentrations following dialysis were not measured, these amounts are expected to be insignificant with respect to drug delivery applications. For example, following an identical dialysis process we found that different block copolymer PNPs showed no significant cytotoxicity, indicating that any remaining DMF amounts were extremely small.[63] A follow-up study will address the question of residual DMF toxicity following dialysis of the PNP materials described in this paper. Bulk samples were prepared in triplicate. Unless otherwise stated, bulk samples were analyzed immediately following dialysis.

Microfluidic Reactor Fabrication. The microfabrication steps followed previously described procedures.[55-67] Firstly, negative masters were fabricated on silicon wafers (Silicon Materials) using the negative photoresist SU-8 100 (Microchem). A 150 μm-thick SU-8 film was spin-coated at 2000 rpm onto the silicon wafer and heated at 65 °C for 12 min and then at 95 °C for 50 min. After the wafer was cooled, a photomask was placed directly above, and the wafer was exposed to UV light for 100 s. Then, the UV-treated film was heated at 65 °C for 1 min and then 95 °C for 20 min. Finally, the silicon wafer was submerged in SU-8 developer (Microchem) and rinsed with isopropanol until all unexposed photoresist was removed.

Microfluidic chips were fabricated from polydimethylsiloxane (PDMS) using a SYLGARD 184 silicon elastomer kit (Dow Corning). For fabrication of all PDMS chips, the elastomer and curing agent were mixed at a 7:1 ratio and degassed under vacuum. The resulting mixture was poured over a clean negative master chip in a Petri dish and further degassed until all remaining air bubbles were removed. The PDMS was heated at 85 °C until cured (~20 min) and then peeled from the negative master; holes were punched through the reservoirs of the resulting PDMS chip to allow for the insertion of tubing. A thin PDMS film (substrate layer) was also made on a glass slide by spin-coating a 20:1 elastomer/curing agent mixture followed by curing. The substrate layer was then permanently bonded to the base of the microfluidic reactor (channel layer) after both components were exposed to oxygen plasma for 45 s. The resulting reactor (Figure 2) has a set channel depth of 150 μm and consists of a sinusoidal mixing channel 100 μm wide and a sinusoidal processing channel 200 μm wide, identical to the reactor described in previous publications from our group.[55-67]

Flow Delivery and Control. The steps of flow delivery and control followed previously described procedures.[55-67] Pressure-driven flow of liquids to the reactor inlet was provided using 1 mL gastight syringes (Hamilton) mounted on syringe pumps (Harvard Apparatus). The microfluidic chip was connected to the liquid syringes via 1/16th-inch (OD) Teflon tubing (Mandel Scientific). Argon (Ar) gas flow was introduced to the chip via an Ar tank regulator and a downstream regulator (Johnston Controls) for fine adjustments. The chip was connected to the downstream regulator through a 1/16th-inch (OD)/100-μm (ID) Teflon tube (Mandel Scientific). The liquid flow rate (Q_{liq}) was programmed via the syringe pumps, and the gas flow rate (Q_{gas}) was fine-tuned via the downstream pressure regulator in order to set the nominal total flow rates (Q) of 50, 100, and 200 μL/min described in the main text. Due to the compressible nature of the gas and the high gas/liquid interfacial tension, discrepancies arise between the nominal (programmed) and actual values of Q_{gas}, $Q_{\mathrm{gas}}/Q_{\mathrm{liq}}$, and the total flow rate (Q_{total}). Therefore, actual values of Q_{gas}, $Q_{\mathrm{gas}}/Q_{\mathrm{liq}}$, and $Q_{\mathrm{total}} = Q_{\mathrm{gas}} + Q_{\mathrm{liq}}$ for each microfluidic experiment were calculated from the average volume of gas bubbles in the microchannels and are reported Table S1. Specifically, three images of the microchannels were captured using a Genie Nano-C1280 camera (1stVision) equipped with an On-Semi Python1300 sensor and a C-Mount Manual Iris Varifocal lens (1/1.8", 4-13mm, *f*/1.5) (Tamron) at each of three different time periods at the beginning, middle, and end of the sample collection process. A typical image of stable two-phase gas-liquid flow during sample collection is shown in Figure S4. Analysis of the gas bubbles and liquid plugs within the microfluidic reactor was achieved using image analysis software (ImageJ), which gives the end-to-end distance of individual gas bubbles and liquid plugs, $L_{\mathrm{gas},i}$ and $L_{\mathrm{liq},i}$, respectively, under a given set of flow conditions. The gas-to-liquid flow ratio, $Q_{\mathrm{gas}}/Q_{\mathrm{liq}}$, was determined from each image as the ratio between measured $\sum_i L_{\mathrm{gas},i}$ and $\sum_i L_{\mathrm{liq},i}$ ($i \geq 150$). Actual gas-to-liquid flow ratios for all experimental runs are reported as average values determined from 9 images (3 images × 3 time points) for each run. All actual Q_{total} values within Table S1 are within 10 % of nominal Q values.

Microfluidic Preparation of DualM PNPs. For microfluidic preparation of DualM PNPs, the following three fluid streams were combined to give stable gas-segmented liquid plugs within the reactor, (1) 1.0 wt % PEO-ss-PHMssEt solution in DMF; (2) pure DMF; and (3) DMF/water. The flow rates of the three liquid streams were equal for all runs, and the water content of the DMF/water stream was selected to yield steady-state on-chip concentrations of 0.33 wt % copolymer and 21.7 wt % water. The critical water content of 0.33 wt % PEO-ss-PHMssEt in DMF was previously determined to be 11.7 ± 0.2 wt %, so that the water content for microfluidic DualM PNP preparation is designated cwc + 10 wt % for all investigated flow rates.

Unless otherwise stated, the PNPs were collected from the chip into vials containing 10× excess by volume of deionized water. In order to remove residual DMF, the resulting PNP dispersions were then immediately transferred into a 6−8 kDa MWCO dialysis membrane (Spectrum Laboratories) and dialyzed against deionized water for at least 18 h, with changing of deionized water every hour for the first 4 h. Microfluidic samples at each flow rate were prepared in triplicate. With the exception of two-week stability tests, all microfluidic samples were analyzed immediately following dialysis.

Determination of Equilibrium PNP Structures. To determine the equilibrium PNP state, the copolymer was dissolved in DMF at an initial polymer concentration of 0.33 wt % then deionized water was added dropwise at a rate of 1 drop every 10 s under rapid stirring to a water content of cwc + 10 wt % (identical to the on-chip water content for all microfluidic preparations). The resulting dispersion was allowed to anneal for 2 weeks in the dark at 23 ºC. To quench the dispersion, it was poured all at once into a 10× excess volume of deionized water with vigorous stirring then finally dialyzed. A drop of both unquenched and quenched dispersion was deposited on transmission electron microscopy (TEM) grids for imaging.

Determining Effects of GSH Incubation on PNP Sizes and Morphologies. GSH-triggered degradation experiments were carried out by incubating DualM PNPs with 1.0×10^{-2} M GSH, in order to mimic the cancerous intracellular environment based on a recent study, which showed GSH concentrations in multiple cancer cell lines varied from 5 mM to 10 mM.[70] Specifically, 2.0 mL of 2.0×10^{-2} M GSH stock solution was added dropwise to 2.0 mL of each PNP dispersion with vigorous stirring. The final concentrations of GSH and PNPs in the mixture were 3.1 mg/mL (1.0×10^{-2} M) and ~0.1 mg/mL, respectively. The resulting dispersion was stirred at 23 °C for 24 h. Changes in hydrodynamic sizes, size distributions, and morphologies during GSH incubation were monitored by dynamic light scattering (DLS) and TEM by taking aliquots of the dispersion for measurement at various incubation times (t = 2 h, 4 h, and 24 h). For DLS measurements, 0.5 mL aliquots were extracted and transferred to a pre-cleaned scintillation vial containing ~5 mL of filtered deionized water (2 × 0.20 μm Nylon syringe filters, National Scientific) to give a final PNP concentration of ~0.01 mg/mL, followed by an immediate DLS measurement. Triplicate DLS measurements were completed within 20 minutes of extracting the aliquot. For TEM measurements, a single drop of dispersion was extracted and deposited onto a TEM grid, followed by uranyl acetate staining, as described in the subsequent section. All GSH incubation experiments were performed within 24 h of sample preparation. PNP samples were stored in the dark in sealed vials before mixing with GSH. To elucidate the effects of other experimental conditions (besides

GSH) on PNP size and morphology, control experiments were also carried out for each PNP sample. In each control experiment, 2.0 mL of deionized water was added dropwise to 2.0 mL of each PNP dispersion with vigorous stirring and the final dispersions (~0.1 mg/mL) were stirred at 23 °C for 24 h, identical to the GSH incubation experiments. DLS and TEM measurements taken immediately after water addition were used to represent the initial time point (t = 0 h) for both control and incubation experiments. Subsequent DLS measurements of the control sample (no GSH) were also taken at t = 2 h, 4 h, and 24 h time points.

Dynamic Light Scattering. DLS measurements were carried out for determination of hydrodynamic sizes, polydispersities, and size distributions of DualM PNPs. DLS experiments were performed on a Brookhaven Instruments photo-correlation spectrometer equipped with a BI-200SM goniometer, a BI-9000AT digital autocorrelator, and a BI-Mini-L30 30 mW red (636 nm) compact diode laser, at a scattering angle of 90° and a temperature of 25 °C. PNP concentrations for all DLS measurements were ~0.01 mg/mL. For each PNP dispersion, mean effective hydrodynamic sizes and polydispersities were determined from three measurements of the autocorrelation function using cumulant analysis. Representative intensity-weighted size distributions were determined from CONTIN analysis. Reported mean effective hydrodynamic sizes and polydispersities for each condition were determined by averaging values from triplicate preparations. Standard errors (σ) on hydrodynamic sizes and polydispersities were calculated from the standard deviation (s) of triplicate values: $\sigma = \frac{s}{\sqrt{3}}$.

Transmission Electron Microscopy. Negatively stained samples for TEM imaging were prepared by depositing a drop of ~0.1 mg/mL DualM PNP dispersion on a Formvar/carbon-coated 200-mesh copper TEM grid (Ted Pella Inc.) followed by a drop of 1 wt % uranyl acetate aqueous solution as a negative staining agent. Excess liquid was immediately removed using lens paper, followed by drying of the remaining liquid under ambient conditions. For unquenched PNP samples either collected from the chip or prepared in the section on the Relaxation of PNPs to Equilibrium Structures, the remaining DMF in the final solutions was found to dissolve the Formvar film, and so the carbon-coated 200-mesh copper TEM grids (Ted Pella Inc.) were used. Imaging was performed on a JEOL JEM-1400 transmission electron microscope, operating at an accelerating voltage of 80 kV and equipped with a Gatan Orius SC1000 CCD camera. Size determinations were carried out using ImageJ from three separate images of different regions of the TEM grid. As morphologies other than spheres (vesicles and cylinders) were less numerous than spheres, non-spherical morphology dimensions were determined from a total of at least 50 PNPs whereas sphere dimensions were determined from a total of $N > 300$. The number percentage of reported morphologies was also measured from three separate images of different regions of the TEM grid using the particle analysis function in ImageJ. Reported uncertainties σ were calculated from the standard deviation s of average dimensions taken from the three images: $\sigma = \frac{s}{\sqrt{3}}$.

The inner hydrophilic compartments of SVs and LVs appeared dark in TEM images due to reverse staining. This allowed spheres to be distinguished from vesicles, since the hydrophobic cores of spheres appeared uniformly bright while SVs and LVs contained one or more dark compartments. For SVs and LVs, the areal percentage of the dark inner compartments relative to the entire particle area was analyzed using ImageJ. Briefly, a cropped image of each selected PNP was adjusted by selecting appropriate contrast, sharpness, and brightness levels. Then boundaries of the PNP and its internal compartments were defined using the binarization function of the software. Finally the total inner compartment area, A_{compart}, and the total PNP area, A_{PNP} were calculated by the software. The relative area of the inner compartments was then calculated for each PNP:

$$RA_{\text{compart}}\ (\%) = \frac{A_{\text{compart}}}{A_{\text{PNP}}} \times 100$$

Reported RA_{compart} values represent averages calculated from $N \geq 50$ PNPs containing compartments selected from at least 3 images taken in different regions of the TEM grid. Reported uncertainties σ were determined by the standard deviation of relative areas for N measured PNPs: $\sigma = \frac{s}{\sqrt{N}}$.

RESULTS AND DISCUSSION

Effect of Flow Rate on Mean Hydrodynamic Sizes and Size Distributions of DualM PNPs. We first investigated the effect of microfluidic flow rate on the PNP hydrodynamic sizes and size distributions determined from DLS. Figure 3A shows effective hydrodynamic diameters ($d_{\text{h,eff}}$) and polydispersities of DualM PNPs prepared using the microfluidic reactor at various flow rates (Q = 50, 100, and 200 μL/min) and using bulk nanoprecipitation (Q = 0 μL/min). All data in Figure 3A were obtained from cumulant analyses of DLS autocorrelation functions. The polydispersity value is a measure of the broadness of the PNP size distribution and is calculated based on the following equation:

$$\text{Polydispersity} = \frac{\mu_2}{\bar{\Gamma}^2}$$

where $\bar{\Gamma}$ and μ_2 describe the first and second moments in the cumulant expansion of the decay rate with respect to delay time, τ.

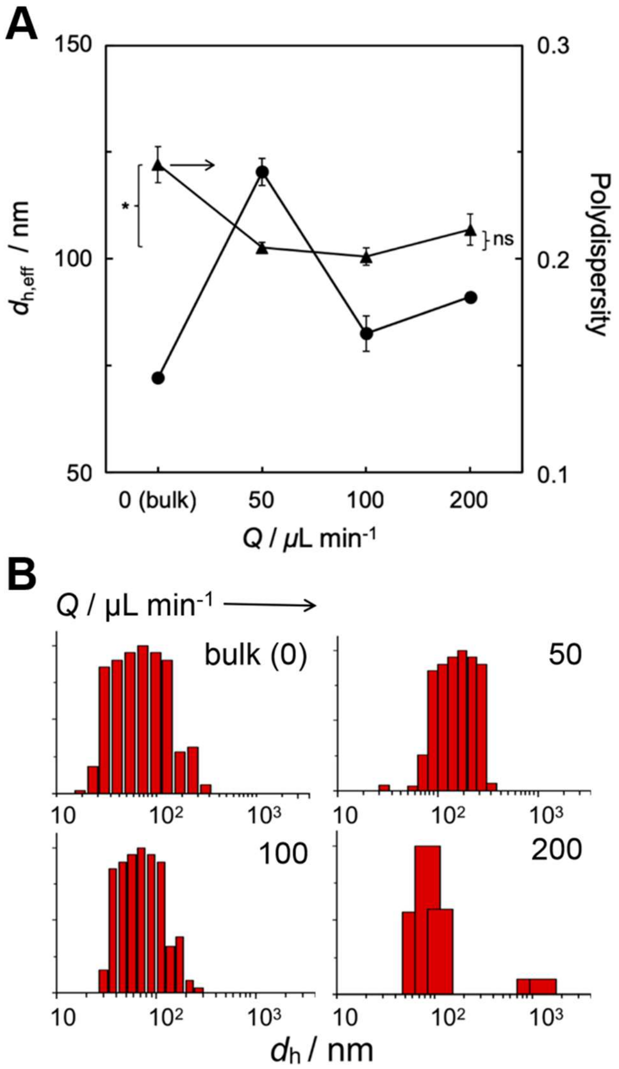

Figure 3. (A) Effect of microfluidic flow rate *Q* on DualM PNP hydrodynamic diameter and polydispersity. (B) CONTIN intensity-weighted size distributions. $Q = 0$ μL/min designates the bulk method of nanoprecipitation. Brackets in (A) indicate statistical comparisons between polydispersities of PNPs generated under different conditions: * indicates $p < 0.05$ and ns indicates $p > 0.05$.

In Figure 3A, we see that all $d_{h,eff}$ values for microfluidic-prepared samples are larger than the bulk value of 72 nm. Within the set of flow-variable microfluidic samples, $d_{h,eff}$ first decreases (from 120 nm to 82 nm) and then increases (from 82 nm to 91 nm) as the manufacturing flow rate increases from $Q = 50$ to $Q = 200$ μL/min. We attribute this nonmonotonic trend to the competing roles of shear-induced particle coalescence and shear-induced particle breakup as PNPs above the cwc circulate through high-shear "hot spots" within the microchannels. Specifically, compared to bulk nanoprecipitation ($Q = 0$ μL/min), the increased shear environment in the microfluidic channels at $Q = 50$ μL/min results in an increase in particle size due to shear-induced coalescence of small PNPs. However, as PNP size increases, the critical capillary number also increases, leading to a dominant contribution from shear-induced breakup. This explains the observed drop in hydrodynamic size between $Q = 50$ μL/min and $Q = 100$ μL/min. Finally, with a further increase in flow rate, the competition between coalescence and breakup leads to a slight increase in $d_{\mathrm{h,eff}}$ between $Q = 100$ μL/min and $Q = 200$ μL/min. Intensity-weighted size distributions for PNPs prepared at different flow rates were obtained from CONTIN analysis of DLS data as shown in Figure 3B.

Along with hydrodynamic sizes, PNP polydispersities are also affected by flow rate as shown in Figure 3A. Specifically, PNP polydispersity decreases significantly between the bulk ($Q = 0$ μL/min) and $Q = 50$ μL/min microfluidic preparations, while further increases in flow rate are not found to change polydispersities significantly. Further insights into the effect of flow rate on polydispersities are provided by considering CONTIN distributions (Figure 3B). Comparison of CONTIN distributions show that the broad spread of small PNPs ($d_{\mathrm{h}} < 100$ nm) that are present in the bulk case is reduced significantly in the microfluidic $Q = 50$ μL/min case. This is explained by exposure of PNPs to the high-shear "hot spots" in the microchannels leading to shear-induced coalescence of smaller particles in the distribution. Similar CONTIN distribution widths are found for $Q = 50$ μL/min and $Q = 100$ μL/min PNPs, consistent with the trend in Figure 3A. Finally, in the CONTIN distribution at $Q = 200$ μL/min, we note the first appearance of a large PNP population (d_h > 1000 nm). Similar polydispersity values at different microfluidic flow rates (Figure 3A) is attributed to the competition between shear-induced coalescence and shear-induced breakup discussed previously.

Effect of Flow Rate on DualM PNP Morphology. Along with hydrodynamic sizes and polydispersities, we find that flow-tunable microfluidic shear forces have a strong effect on the morphologies of DualM PNPs. Figure 4 shows representative TEM images of PNPs prepared in the bulk (“zero flow” condition) and in the microfluidic reactor at different flow rates. Within these images, the uranyl acetate staining agent is selectively bonded to the PEO coronal chains, providing reverse contrast for the bright hydrophobic PHMssEt cores. Table 1 lists the observed morphologies, mean core dimensions, and number percentages of reported morphologies, determined from statistical analysis of multiple TEM images for each sample.

As shown in Figure 4A and Table 1, the bulk nanoprecipitation method of PNP manufacturing gives rise to a large majority (98%) of spheres with mean core diameter of 68 nm. Also present in the bulk sample are a small number of two types of vesicles (Figure 4A, inset): 1. small vesicles (d < 100 nm), which unlike spheres contain a distinct small spherical compartment (SVs, white arrow) and 2. large vesicles (d > 100 nm) containing either large spherical compartments or one or more cylindrical compartments (LVs, dashed white circles). These two vesicles types each constitute ~1% of the total number of PNPs formed in the bulk (Table 1).

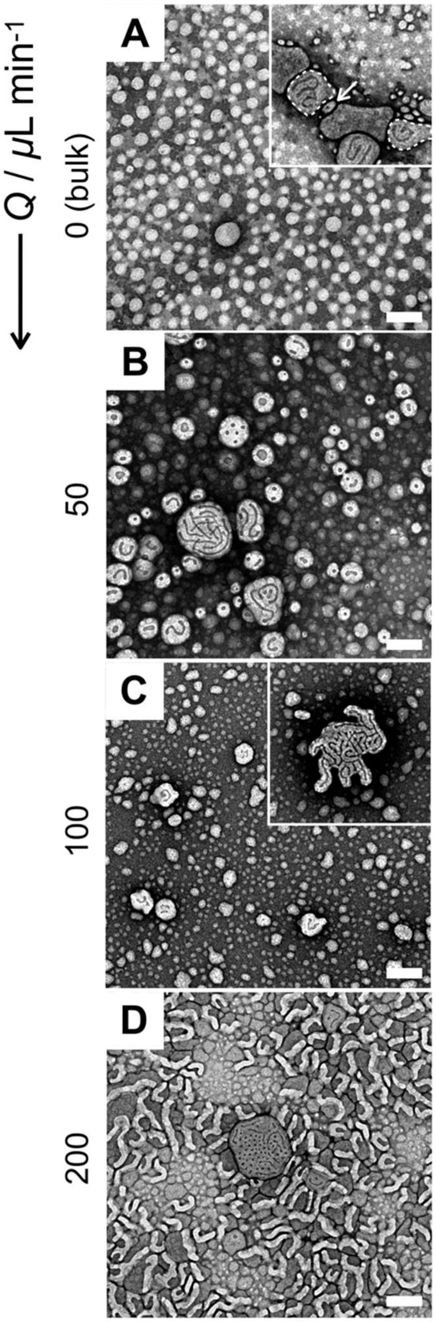

Figure 4. Effect of microfluidic flow rate *Q* on the morphologies of DualM PNPs. Representative TEM images for PNPs formed at (A) *Q* = 0 μL/min (bulk); (B) *Q* = 50 μL/min; (C) *Q* = 100 μL/min; and (D) *Q* = 200 μL/min. White arrows and white dashed circles in (A) indicate examples of SVs and LVs, respectively. All scale bars are 200 nm; main images and insets share the same scale bar.

Table 1. Morphologies,[a] Mean Dimensions,[b] and Number Percentages for DualM PNPs Manufactured Using Bulk and Microfluidics at Variable Flow Rate

Q / μL min^{-1}	Morphology	Dimension / nm	Number Percentage / %
0 (bulk)	S	68 ± 5	98.5 ± 0.4
	SV	60 ± 4	1.1 ± 0.2
	LV	233 ± 12	1.4 ± 0.1
50	S	69 ± 9	79 ± 3
	SV	69 ± 5	18.1 ± 0.2
	LV	185 ± 15	3 ± 1
100	S	38 ± 4	99.5 ± 0.3
	SV	65 ± 7	0.5 ± 0.1
	LV	159 ± 15	0.5 ± 0.2
200	S	47 ± 4	55 ± 2
	SV	52 ± 10	1.5 ± 0.1
	LV	291 ± 81	2.3 ± 0.4
	C	31 ± 2	42 ± 3

[a]Morphologies are indicated as S (spheres), SV (small vesicles), LV (large vesicles), or C (cylinders). [b]Dimensions refer to sphere and small vesicle diameters and cylinder widths determined from TEM images. For non-spherical large vesicles, dimensions refer to the longest measurable internal distance. Standard errors are reported to represent the uncertainty of mean dimensions and number percentages determined from triplicate images in different regions of the TEM grid.

Compared to the bulk-prepared PNPs, we find a number of interesting differences in the observed morphologies when PNPs are manufactured in the microfluidic reactor at the lowest on-chip flow rate (Q = 50 μL/min, Figure 4B). First, the percentage of SVs increases dramatically from 1% to 18% (Table 1). Second, the percentage of LVs increases from 1% to 3%; considering the much larger dimensions of LVs compared to SVs and spheres, this small percentage increase explains the corresponding sharp increase in intensity-averaged hydrodynamic diameter observed by DLS between Q = 0 μL/min (bulk) and Q = 50 μL/min (Figure 3A). Third, mean relative internal compartment areas of SVs and LVs were determined from TEM image analysis (*Supporting Information*, Figure S5), revealing an expansion of inner compartments between the bulk and the Q = 50 μL/min case (*Supporting Information*, Figure S6). Finally, there is a marked increase in the complexity of the inner compartments at Q = 50 μL/min (Figure 5), both in terms of the mixture of highly interconnected cylindrical compartments and discrete spherical compartments, and in the appearance of numerous LVs with one or more planes of mirror symmetry (examples highlighted with dashed white circles, Figure 5). The presence of mirror symmetry in polymer nanoparticles has been previously attributed to nonergodicity and local free energy minimization via chain rearrangements within individual PNPs.[71]

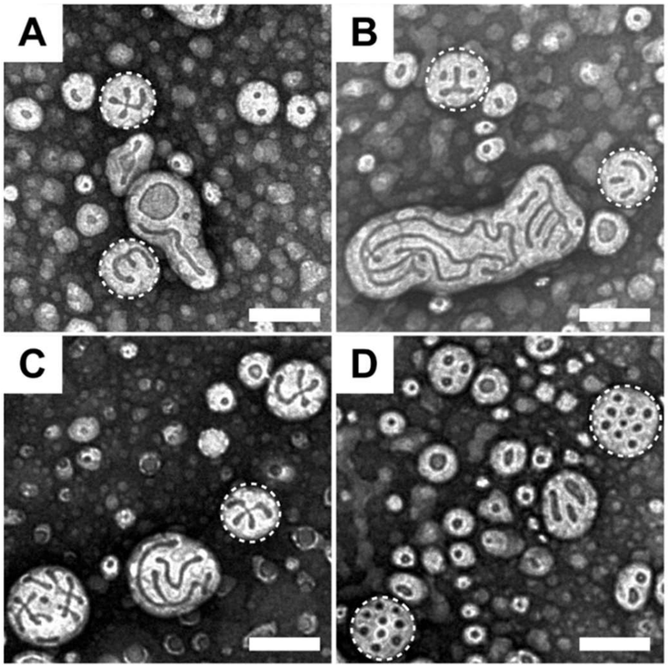

Figure 5. Examples of various LV internal compartment structures formed at Q = 50 μL/min (A−D). White dashed circles highlight LVs with one or more planes of mirror symmetry. All scale bars are 200 nm.

Increasing the microfluidic flow rate to Q = 100 μL/min (Figure 4C) induces further changes in the observed PNP morphologies compared to the Q = 50 μL/min case. When the flow rate is increased, the percentage of SVs (18%) drops dramatically to <1% (Table 1). The percentage of LVs also decreases from 3% to <1%, which likely explains to the corresponding drop in the intensity-averaged hydrodynamic diameter (Figure 3A). At the same time, the percentage of spheres, which are smaller than those formed in the bulk and at Q = 50 μL/min (38 nm, Table 1), increases to 99%. In addition, TEM images reveal that the SVs and LVs become irregularly shaped (Figure 4C), while quantitative image analysis shows that the relative area of their inner compartments contract compared to vesicles observed at the lower flow rate (*Supporting Information*, Figure S6).

Finally, the increase in the flow rate from Q = 100 μL/min to Q = 200 μL/min gives rise to the first appearance of cylinders (Figure 4D), which represent a significant percentage (42%, Table 1) of the morphology mixture. At the same time, the percentage of spheres drops sharply (from 99% to 55%) while the percentage of LVs increases from <1% to 2% and their mean size increases by a factor of 2 (from 159 to 291 nm). We also note that the hydrophilic compartments of LVs formed at Q = 200 μL/min are much less interconnected than at any of the previous flow conditions, including the bulk preparation. This is evidenced by the number of discrete compartments per LV at the various flow rates (*Supporting Information*, Figure S6, inset), which jumps sharply from <2 to ~10 at Q = 200 μL/min. A typical "raspberry-like" LV formed at Q = 200 μL/min with a large number of discrete cylindrical and spherical compartments is shown at the center of the image in Figure 4D. This can be contrasted to "sponge-like" LVs with interconnected compartments formed at Q = 50 μL/min (Figure 4B).

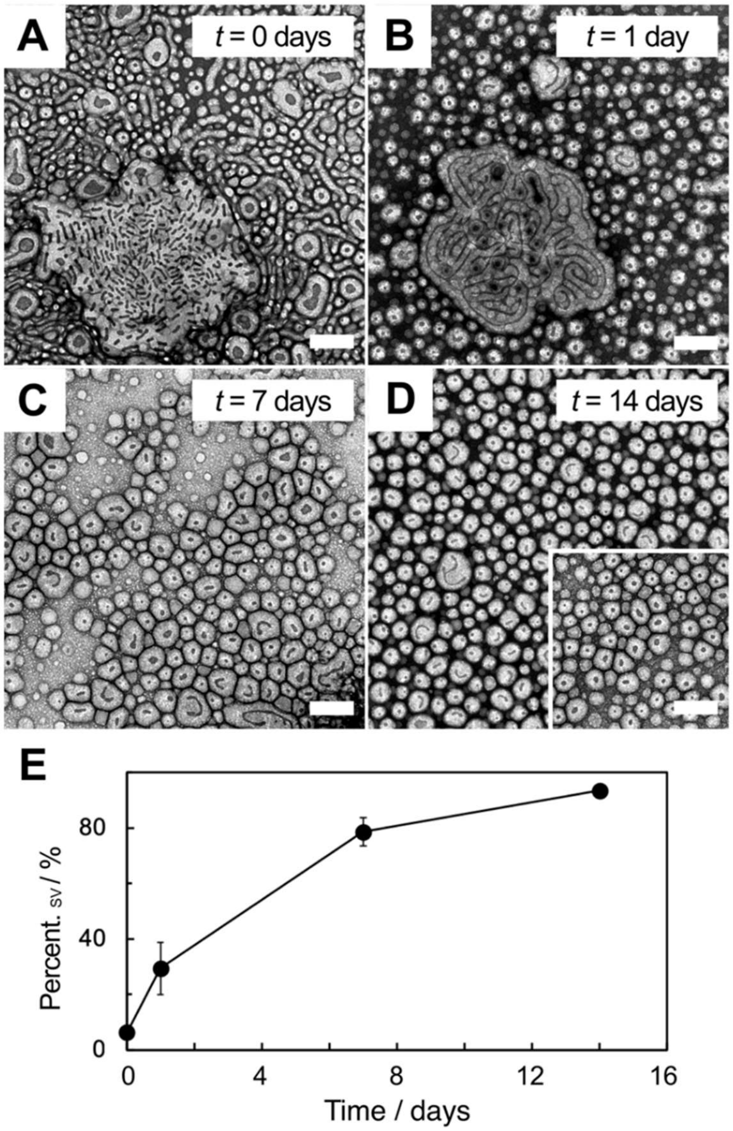

Figure 6. Off-chip relaxation of DualM PNPs formed at *Q* = 200 μL/min without quenching into excess water. TEM images (A−D) were taken at various times after collection showing increasing predominance of SVs. For comparison, a TEM image of mainly SVs formed under equilibrium PNP formation (drop-wise water addition followed by 14-day annealing) is shown in inset of (D). The number percentage of SVs plotted vs. off-chip relaxation time is shown in (E). All scale bars are 200 nm.

Kinetic Stability and Thermodynamic Equilibration of Shear-Induced DualM PNPs. As demonstrated previously for microfluidic formation of shear-induced morphologies, we find that the off-chip stability of DualM PNPs depends strongly on removal of organic solvent following collection from the microfluidic reactor.[55,60] All PNPs described in the previous sections were collected into an excess of pure water followed by removal of the organic solvent by dialysis (quenched condition). We tested the long-term stability of quenched PNPs by comparing TEM and DLS data of Q = 50 μL/min and Q = 200 μL/min samples immediately after dialysis (t = 0 days) and two weeks after dialysis (t = 14 days). PNPs prepared under both flow conditions showed qualitatively similar morphologies after two weeks (*Supporting Information*, Figure S7, A-D). The DLS mean hydrodynamic diameter decreased slightly (by ~13%) for the Q = 50 μL/min sample but remained constant for the Q = 200 μL/min sample over the two week period. Quantitative analysis of TEM images from Q = 50 μL/min and Q = 200 μL/min samples showed that the dimensions of the various morphologies were consistent after two weeks, although we found small but significant changes in the percentages of the various morphologies over that time period (Table S2).

Next, we investigated the off-chip stability of shear-induced PNPs without quenching into an excess of water. For these experiments, a representative PNP sample prepared at the Q = 200 μL/min flow rate was collected into an empty vial so that the water content after collection was the same as the on-chip water content (unquenched condition). We then monitored changes by TEM at different times after collection from the chip (t = 0, 1, 7, and 14 days; Figure 6, A-D). Statistical analysis of the dimensions and number percentages of various morphologies at the various time points are presented in Table 2, along with values for the quenched Q = 200 μL/min PNPs for comparison. We note that the quenched sample represents the PNP state immediately upon collection, whereas the unquenched sample at t = 0 days represents an off-chip relaxation time of ~20 minutes, which was the required preparation time between collection and sample deposition on the TEM grid. We find that the t = 0 sample (Figure 6A) qualitatively resembles the corresponding quenched Q = 200 μL/min sample (Figure 4D) with mixtures of spheres, cylinders, SVs and LVs of comparable dimensions. However, quantitative analysis of TEM images (Table 2) reveals important differences between these samples, including an increase in the percentage of SVs from 1.5% (quenched) to 6% (t = 0 days, unquenched). We also note that whereas many of the larger LVs in the quenched sample contain multiple, mostly spherical, compartments (Figure 4D), these have elongated to short cylindrical compartments in the unquenched t = 0 days sample (Figure 6A).

Table 2. Time-Dependent Morphologies,[a] Mean Dimensions,[b] and Number Percentages for Unquenched DualM PNPs Manufactured On-Chip at $Q = 200$ μL/min

t / day	Morphology	Dimension / nm	Number Percentage / %
quenched	S	47 ± 4	55 ± 2
	SV	52 ± 10	1.5 ± 0.1
	LV	291 ± 81	2.3 ± 0.4
	C	31 ± 2	42 ± 3
0	S	60 ± 4	59 ± 6
	SV	68 ± 2	6 ± 1
	LV	282 ± 38	4 ± 1
	C	36 ± 3	31 ± 8
1	S	47 ± 2	70 ± 10
	SV	73 ± 1	30 ± 10
	LV	234 ± 18	1.7 ± 0.3
7	S	56 ± 5	15 ± 5
	SV	74 ± 4	79 ± 5
	LV	201 ± 7	6 ± 9
14	S	46 ± 9	1.5 ± 0.3
	SV	64 ± 1	94 ± 2
	LV	130 ± 2	4 ± 2

[a] Morphologies are indicated as S (spheres), SV (small vesicles), LV (large vesicles), or C (cylinders). [b] Dimensions refer to sphere and small vesicle diameters and cylinder widths determined from TEM images. For non-spherical large vesicles, dimensions refer to the longest measurable internal distance. Standard errors are reported to represent the uncertainty of mean dimensions determined from triplicate images in different regions of the TEM grid.

Figure 6 and Table 2 also show marked changes in the unquenched PNPs over time on the time scale of days. After one day ($t = 1$ day, Figure 6B) the sample no longer contains cylinders and the percentage of SVs has increased sharply from 6% to 30% (Figure 6E). In addition, the short cylindrical compartments of LVs have further elongated to become highly interconnected. Figure S8 (*Supporting Information*) shows multiple TEM images of LVs from the quenched, $t = 0$ days (unquenched) and $t = 1$ day (unquenched) samples, highlighting the transition of LVs from discrete spherical to discrete cylindrical to interconnected cylindrical compartments. After one week ($t = 7$ days, Figure 6C) the PNP morphologies further develop such that there are no longer LVs with interconnected cylindrical compartments and the percentage of SVs has increased to 79% (Figure 6E). Finally, after two weeks ($t = 14$ days, Figure 6D), almost all of the PNPs are ~60 nm SVs (94%) with only a few residual LVs and spheres observed in the TEM images.

The observed relaxation of unquenched PNPs to mostly SVs over two weeks indicates that the shear-induced morphologies formed at variable flow rate in the microfluidic channels are thermodynamically unstable under off-chip quiescent conditions. Furthermore, the predominance of SVs after two weeks equilibration (Figure 6D) suggests that SVs represent the Gibbs free energy minimum at the on-chip water content of cwc + 10 wt %. To confirm this, we also prepared PNPs by slow drop-wise water addition to a 0.33 wt % copolymer solution in DMF up to cwc + 10 wt %, followed by equilibration for two weeks. This experiment allowed us to reach the equilibrium state by slowly increasing the water content from the dynamic initial state of copolymer single chains. TEM of the resulting PNPs (Figure 6D, inset) revealed a vast majority of SVs (96 ± 3%) with mean diameter 62 ± 2 nm, confirming SVs to be the equilibrium morphology. Despite the thermodynamic instability of the shear-induced morphologies, our stability test of quenched PNPs reveals that the observed off-chip relaxation is slowed significantly by a sudden increase in water content followed by overnight dialysis. The relative kinetic stability of the quenched morphologies over two weeks points the feasibility of testing flow-dependent GSH responsivity in these samples. Finally, we note that the observed evolution of LV inner compartments from discrete spherical to discrete cylindrical to interconnected cylindrical (Figure S8) suggests a possible relaxation mechanism from LVs to equilibrium SVs. In the next section, we propose that a similar rearrangement pathway is also part of the complex interplay of thermodynamics and kinetics in shear-directed DualM PNP formation.

Discussion of Shear-Directed Microfluidic PNP Formation from DualM Copolymer. The effects of flow rate on the sizes and morphologies of DualM PNPs reported in the previous sections point to the important role of high shear on PNP formation within the microfluidic channels. Previous work from our group on block copolymer self-assembly in two-phase gas-liquid microfluidic reactors has demonstrated that PNP circulation through high-shear hot-spots within the microchannels strongly influences the final morphologies through an interplay of shear-induced coalescence, shear-induced break-up, and intraparticle chain rearrangements.[55,58] However, the detailed mechanism of on-chip morphology formation could not be elucidated in those previous studies, due to an absence of recognizable intermediate structures within the final PNP samples. In contrast, we find that the DualM copolymer investigated in this work gives rise to unique flow-dependent PNP mixtures that include complex morphologies identifiable as kinetically trapped intermediates between shear-dependent states. Careful qualitative and quantitative analysis of the resulting morphologies allows us to propose the most detailed mechanism to date of microfluidic PNP formation in the presence of flow-variable high shear.

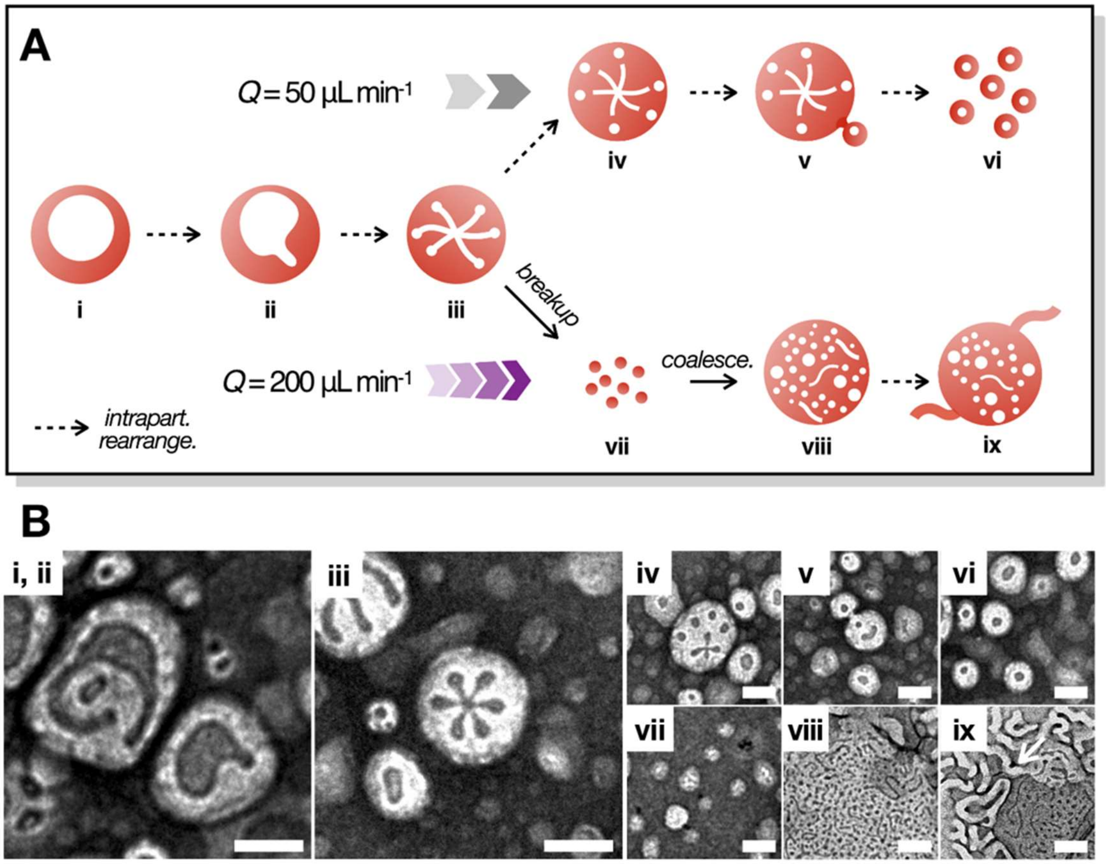

Figure 7. (A) Schematic of proposed mechanisms of flow-directed morphological transitions and (B) TEM images of the intermediate PNPs represented in (A). In (B), TEM images of structures (i) - (vi) are from Q = 50 μL/min sample, while images of structures (vii) - (ix) are from Q = 200 μL/min sample. All scale bars are 100 nm.

Figure 7 outlines the proposed mechanisms of flow-dependent morphological transitions (Figure 7A). The accompanying TEM images in Figure 7B show specific PNPs collected at the indicated flow rates which are kinetically trapped intermediate structures evincing various stages of the mechanisms in Figure 7A. Of the four PNP preparation conditions, the microfluidic low-flow rate case (Q = 50 μL/min) shows the highest percentage of the equilibrium morphology of SVs. The source of these SVs appears to be the numerous LVs with complex internal structure found at this flow rate. In the proposed mechanism, LVs start with a single large spherical compartment (i), then undergo a series of spontaneous intraparticle rearrangements in order to generate low-free energy SVs. First, the large spherical compartments distort and pinch off cylindrical-shaped appendages (ii). These appendages evolve into an interconnected network of cylindrical compartments, often with mirror symmetry, with cylindrical arms extending outwards, towards the interface of the PNP core (iii). The internal curvature of cylindrical arm caps increases until a small spherical compartment breaks off from the end of each arm, leading to multiple discrete compartments situated near the LV core interface (iv). Finally, these small compartments bud off from the LV core (v) to form multiple SVs (vi).

At higher flow rates, the intraparticle rearrangement pathway from LVs to SVs described above is interrupted by the interplay of shear-induced breakup (Q = 100 μL/min and Q = 200 μL/min) and shear-induced coalescence (Q = 200 μL/min) events, activating an alternate rearrangement pathway to form cylinders. Starting at Q = 100 μL/min, the maximum shear rate increases such that PNPs above a critical size, including LV-to-SV intermediates, exceed their critical capillary number and undergo shear-induced breakup to form mainly small spheres (vii). Finally, at the highest flow rate (Q = 200 μL/min), the maximum shear rate is sufficiently high to induce shear-induced coalescence of small spheres to form a new population of LVs (viii), despite continued competition with shear-induced breakup.

In contrast to sponge-like LVs found at Q = 50 μL/min (iii), which develop highly interconnected internal compartments, raspberry-like LVs at Q = 200 μL/min (viii) contain a large number of small discrete compartments. We believe that this raspberry-like internal structure arises from the random collision and coalescence of small spheres, resulting in hydrophilic coronal chains being internalized and forming discrete domains dispersed throughout the LV core. Unlike the slow evolution of LVs found at $Q = 50$ μL/min (i – v), competition with shear-induced breakup prevents raspberry-like LVs (viii) from following the relaxation pathway to equilibrium SVs. Instead, these LVs appear to lower their free energy *via* an alternate pathway, spinning cylindrical PNPs from their surfaces (ix). An example of a cylinder evolving from a raspberry-like LV is indicated by a white arrow in Figure 7B(ix).

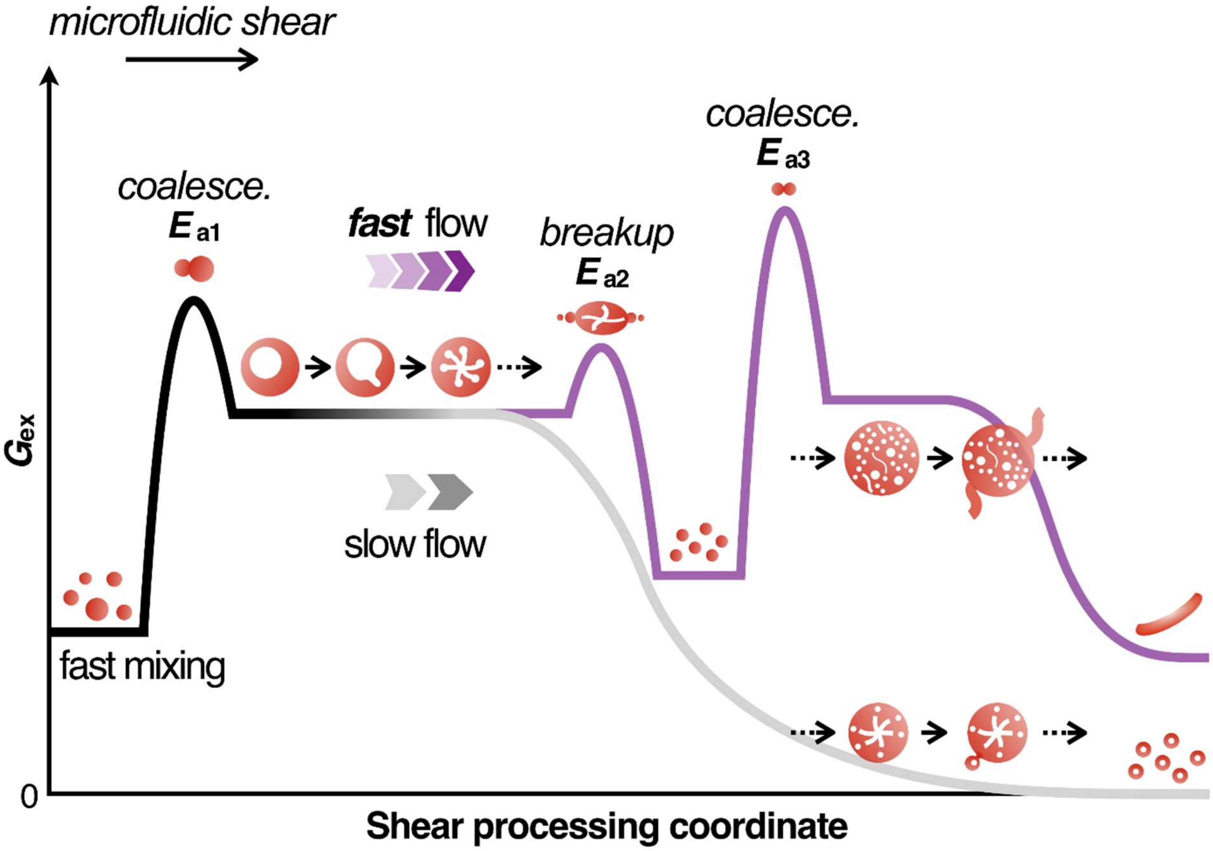

Figure 8. Energy diagram depicting formation and shear processing of DualM PNPs in the microfluidic reactor under different flow conditions.

Figure 8 presents a qualitative free energy diagram summarizing the interplay of shear-induced coalescence, shear-induced breakup, and intraparticle chain rearrangements, in the generation of flow-dependent PNP morphologies from the DualM copolymer. We note that the proposed shear-induced formation pathways described in Figures 7 and 8 were not observed directly in real time, but rather were deduced from the various mixtures of kinetically-trapped transition morphologies at different flow rates. Such deductions of time-dependent processes from static TEM images require the assumption that PNPs observed off-chip correspond to snapshots of dynamic on-chip structures, from which a time sequence can be postulated. More direct time-dependent mechanistic evidence could possibly be obtained using redesigned chips allowing samples to be collected at different distances along the processing channel (Figure 2), where distance would be correlated to shear exposure time, although such experiments were beyond the scope of the present study. For all microfluidic preparations, we assume that fast mixing with water early in the microchannel gives rise to non-equilibrium spheres (~70 nm), similar to those formed by bulk nanoprecipitation (Table 1). In the slow flow case ($Q = 50\ \mu$L/min), shear-induced coalescence of spheres generates intermediate LVs within the hot spots, as shear forces overcome the activation barrier $E_{a1.}$ These LVs then undergo intraparticle rearrangements as they relax to equilibrium SVs. As a result, PNPs formed at $Q = 50\ \mu$L/min contain a significant percentage of SVs (18%), along with intermediate LVs (3%), and the original spheres (79%).

In the fast flow cases ($Q = 100\ \mu$L/min and $Q = 200\ \mu$L/min), the increased shear rate activates shear-induced breakup of LVs and other particles exceeding the critical capillary number, interrupting the relaxation pathway to equilibrium SVs. At $Q = 100\ \mu$L/min, the system is kinetically trapped in a high-excess free energy state in between the activation barriers E_{a2} and E_{a3}, where the vast majority of PNPs are small spheres (99%). Due to shear-induced particle breakup to the right of E_{a2}, spheres formed in fast flow rate cases are smaller (~40 nm) than spheres formed under slow flow conditions (~70 nm). Finally, at the highest investigated flow rate, $Q = 200\ \mu$L/min, the maximum shear rate increases again such that the activation barrier E_{a3} can be overcome, allowing some small spheres to coalescence to form raspberry-like LVs with multiple discrete compartments. Competition with shear-induced breakup prevents these LVs from following the same relaxation pathway to SVs that predominates under slow flow conditions. Instead, these LVs follow an alternate relaxation pathway to form cylinders (42%), which coexist with the intermediate LVs (3%) and small spheres (55%) at Q = 200 μL/min.

Microfluidic Flow Dependence of GSH-Triggered PNP Degradation. Next, the four PNP samples prepared in the bulk and at three microfluidic flow rates (Q = 50, 100, and 200 μL/min) were incubated in 1.0×10^{-2} M GSH and monitored over 24 h by conducting DLS and TEM measurements at the following time points: t = 0, 2, 4, and 24 h (Figure 9). Accompanying controls involved DLS measurements at the same time points for each PNP sample incubated under the same conditions but without GSH.

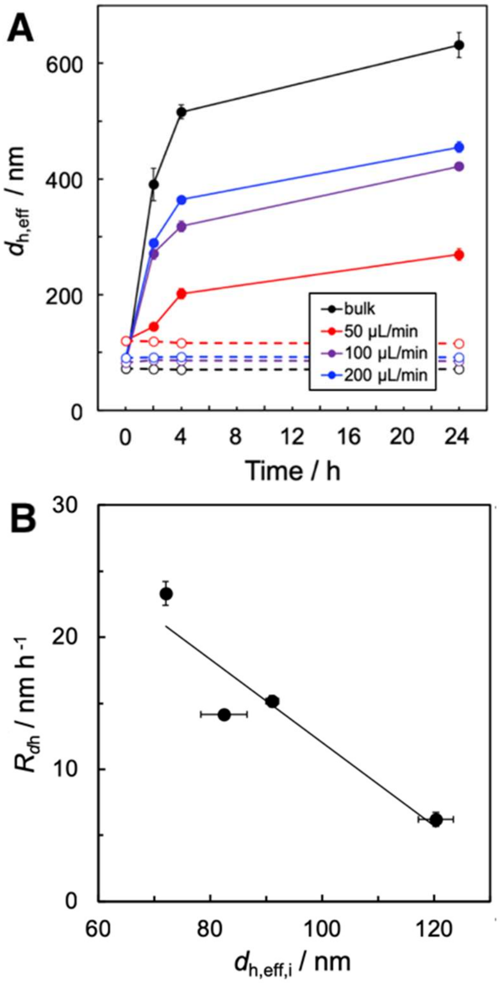

Figure 9. GSH-triggered size increase for bulk and microfluidic DualM PNPs formed at different flow rates, Q. (A) DLS hydrodynamic diameter ($d_{h,eff}$) vs. GSH incubation time. Corresponding open symbols indicate control experiments without added GSH. (B) Average growth rate R_{dh} vs. initial $d_{h,eff}$; the linear regression trend line is shown as black line.

Figure 9A shows DLS effective hydrodynamic diameters at the various time points. All samples in GSH show increases in hydrodynamic size over time, while the control samples (without GSH) show consistent sizes over the 24 h period, confirming the GSH-triggered response. The rate of size increase was found to change over the 24 h incubation period for all four samples, with faster increase in the first 4 hours and slower increase in the subsequent 20 h. However, the total GSH-triggered PNP growth appears to depend strongly on the microfluidic flow conditions of sample preparation. Specifically, PNP samples with smaller initial hydrodynamic sizes (before GSH exposure, $d_{\mathrm{h,eff,i}}$; $t = 0$ h) show more extensive growth over 24 h of GSH exposure. To quantify this, we determined the average rate of growth in $d_{\mathrm{h,eff}}$, $R_{d\mathrm{h}}$ for each sample:

$$R_{dh} = \frac{d_{\mathrm{h,eff,f}} - d_{\mathrm{h,eff,i}}}{24\ \mathrm{h}}$$

and then plotted $R_{d\mathrm{h}}$ versus $d_{\mathrm{h,eff,i}}$. The resulting plot (Figure 9B) fits a linear trend line reasonably well with a negative slope of $-0.32 \pm 0.08\ \mathrm{h}^{-1}$.

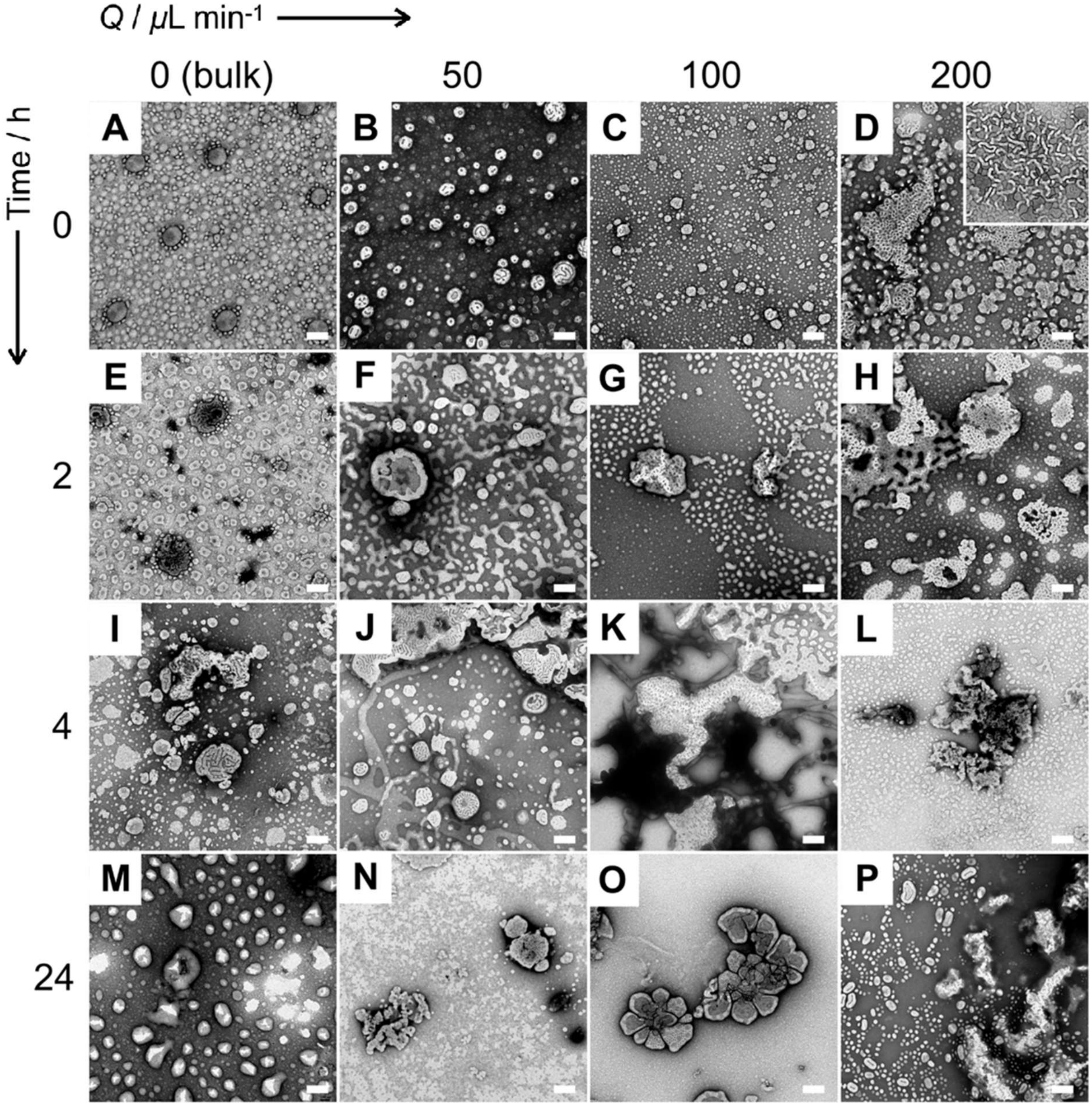

Figure 10. Time-dependent effects of GSH exposure on flow-directed DualM PNP morphologies. Representative TEM images of DualM PNPs formed at (A) *Q* = 0 *μ*L/min (bulk); (B) *Q* = 50 *μ*L/min; (C) *Q* = 100 *μ*L/min; and (D) *Q* = 200 *μ*L/min, at four different time points of GSH exposure at (A−D) 0 h; (B−H) 2h; (I−L) 4 h; and (M−P) 24 h. All scale bars are 200 nm; main images and insets share the same scale bar.

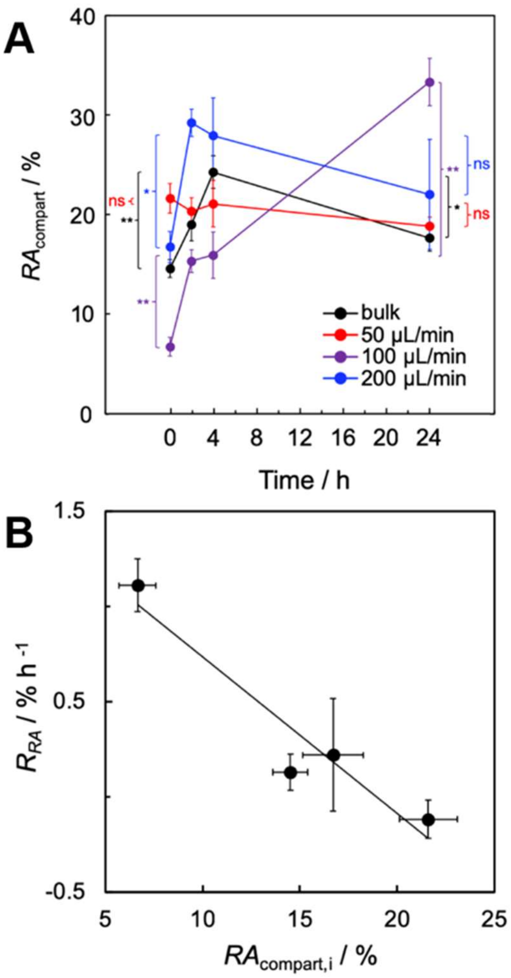

Figure 11. GSH-triggered RA_{compart} increase for bulk and microfluidic DualM PNPs formed at different flow rates, Q. (A) RA_{compart} from TEM images vs. GSH incubation time. (B) Average growth rate R_{RA} vs. initial RA_{compart}; the linear regression trend line is shown as black line. Brackets in (A) indicate statistical comparisons between RA_{compart} values at different time points of GSH exposure: ** indicates $p < 0.005$, * indicates $p < 0.05$ and ns indicates $p > 0.05$.

Next, we determined the time-dependent effects of GSH exposure on PNP morphologies from TEM images. Figure 10 shows representative TEM images of the four investigated samples at each of the four incubation times. For each sample, the TEM images support the increases in size over 24 h observed by DLS. In addition to an overall increase in PNP size, the images reveal that the internal structure of the PNPs is strongly affected by GSH exposure. Specifically, we observe a general increase in the relative area of the dark inner regions in the TEM images with GSH exposure time, corresponding to an increase in the relative volume of the hydrophilic inner PNP compartments.

To quantify the increase in the inner compartment volume upon GSH exposure, we calculated mean relative compartment areas RA_{compart} from multiple TEM images for each time point, then plotted RA_{compart} versus GSH exposure time (Figure 11A). Similar to d_{h} values, we find that RA_{compart} growth with GSH exposure time depends strongly on the PNP preparation conditions, including microfluidic flow rate. In this case, the $Q = 50$ μL/min sample shows the smallest growth and the $Q = 100$ μL/min sample shows the greatest growth in RA_{compart} over the 24 h incubation time. Both the bulk and $Q = 200$ μL/min samples show intermediate overall changes in RA_{compart}, with both of these samples showing an initial increase in the first 4 h followed by a decrease in the subsequent 20 h. To obtain further insight into the dependence of GSH-triggered RA_{compart} growth on the initial PNP structure, we determined the average rate of growth in RA_{compart}, R_{RA} for each sample:

$$R_{RA} = \frac{RA_{\text{compart,f}} - RA_{\text{compart,i}}}{24\ \text{h}}$$

and then plotted R_{RA} versus $RA_{\text{compart,i}}$. We again obtain a straight line plot (Figure 11B), from which the linear trend line yields a negative slope of –0.08 ± 0.02 h^{-1}.

By tracking time-dependent changes in both $d_{\mathrm{h,eff}}$ (Figure 9) and RA_{compart} (Figure 11) upon GSH exposure, it is possible to at least partly separate disulfide cleavage kinetics at the junction (Figure 12A) and pendant (Figure 12B) linkages, respectively. For example, the majority of junction linkages are on the outer surfaces of the PNP cores attached to stabilizing hydrophilic blocks. When these linkages cleave in the presence of GSH, hydrophilic blocks will detach from the cores, leading to surface instability and PNP coalescence, increasing $d_{\mathrm{h,eff}}$ over time (Figure 12A). In contrast, the majority of pendant linkages are embedded in the hydrophobic regions of the PNP cores. When these linkages cleave in the presence of GSH, the hydrophobic blocks become more hydrophilic and phase separate from the uncleaved regions of the core, leading to growing hydrophilic compartments, increasing RA_{compart} over time (Figure 12B). Of course, plots of $d_{\mathrm{h,eff}}$ (Figure 9A) and RA_{compart} (Figure 11A) versus time also include other kinetic contributions from numerous processes on different time scales, including polymer and particle diffusion, phase separation, and particle coalescence, and therefore do not directly provide reaction kinetics for the junction and pendant cleavage reactions, respectively. Analytical techniques such as GPC and NMR that allow for the characterization of degraded products can be used to monitor quantitatively the cleavage of junction and pendant disulfide linkages as a function of incubation time with the reducing agent, although purification and chemical analysis by these methods is not straightforward.[50] However, due to the primary roles of the GSH-triggered junction and pendant cleavage reactions in driving the nanoscale time-dependent processes in Figures 9A and 11A, respectively, the current TEM and DLS analyses provide important insights into the specific roles of microfluidic shear on the GSH-triggered response at both cleavable linkage locations. Additionally, unlike the analytical techniques described in ref. 50, the current analysis directly correlates the chemical response of disulfide linkages to time-dependent changes in PNP sizes and morphologies, which is essential information for the future understanding the transport and function of DualM PNPs in living systems.

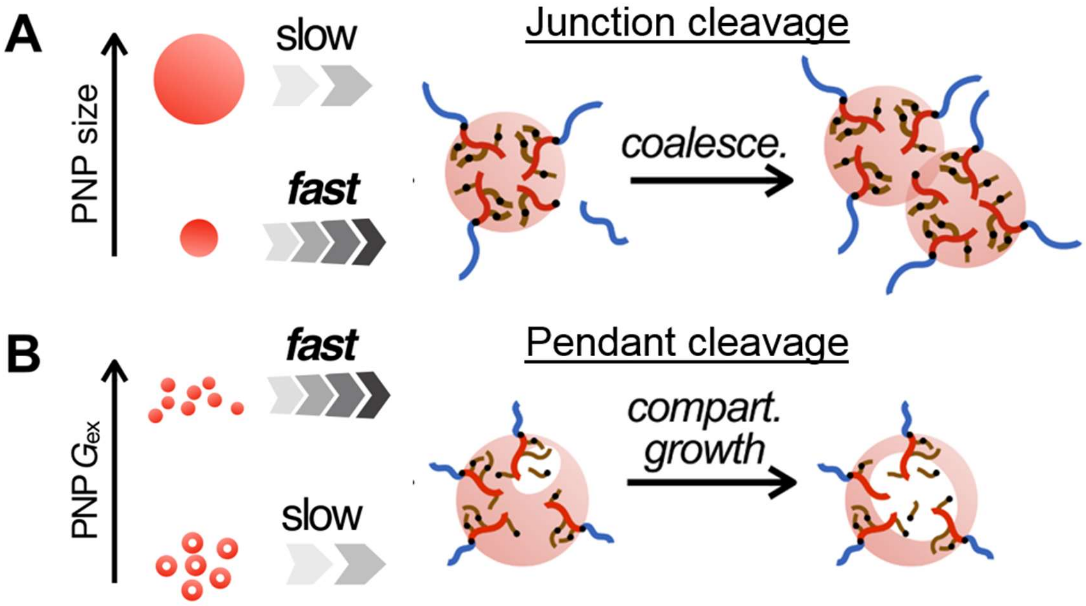

Figure 12. Schematic depicting (A) PNP size dependence of junction disulfide cleavage and (B) PNP excess Gibbs free energy (G_{ex}) dependence of pendant disulfide cleavage.

Figure 9B shows that the rate of GSH-triggered $d_{h,eff}$ growth, R_{dh}, decreases as the initial hydrodynamic size of PNPs increases. This is explained by a decrease in the surface area of the core-corona interface of PNPs leading to a decrease in the exposure of cleavable junction linkages to GSH in the surrounding medium. This suggests that mean PNP size is the primary figure of merit governing the rate junction cleavage in DualM PNPs. Therefore flow rates giving smaller PNP sizes lead to faster junction cleavage (Figure 12A). In contrast, no comparative trend was found when the average rate of GSH-triggered compartment growth, R_{RA}, was plotted against initial hydrodynamic size (*Supporting Information*, Figure S9). However, as shown in Figure 11B, R_{RA} was found to decrease in an approximately linear manner as the initial relative compartment area from TEM images, $RA_{compart,i}$ (proportional to the relative compartment volume) increased.

Unlike the relationship between $R_{d\mathrm{h}}$ and $d_{\mathrm{h,eff,i}}$, (Figure 9B), this cannot be a simple surface area effect, since the exposure of pendant linkages in the hydrophobic regions to GSH would increase, not decrease, as the compartment volume increases. Rather, we attribute this trend to the correlation between RA_{compart} and the excess Gibbs free energy of shear-directed PNPs. As represented in the energy diagram in Figure 8, the lowest-G_{ex} PNPs are SVs, which form predominantly at the flow rate $Q = 50$ μL/min, also corresponding to the highest value of RA_{compart} (*Supporting Information*, Figure S6). Conversely, the highest-G_{ex} PNPs are mainly small spheres formed *via* shear-induced breakup (Figure 8); these are formed at $Q = 100$ μL/min, which also gives the lowest value of RA_{compart} (Figure S6). Bulk and $Q = 200$ μL/min samples are associated with intermediate G_{ex} values (Figure 8) and result in similar, intermediate values of RA_{compart} (Figure S6). We tentatively ascribe the observed inverse relationship between RA_{compart} and G_{ex} to the role of multi-compartment LVs in the relaxation mechanism to low-energy SVs (Figure 7). As exemplified by the $Q = 50$ μL/min case, an increase in the prominence of multi-compartment LVs tends to increase RA_{compart} while also providing a pathway to low-energy SVs, thus decreasing G_{ex}. We conclude that G_{ex}, describing both the PNP size and internal molecular configuration, is the primary figure of merit governing the rate of pendant cleavage in DualM PNPs. Therefore microfluidic flow rates giving PNPs of higher G_{ex} (or lower RA_{compart}) lead to faster pendant cleavage (Figure 12B).

Our studies of various PNP systems in segmented microfluidic reactors have shown that on-chip shear processing can direct both the mean size and internal structure (including morphologies and core crystallinities) of PNPs formed in the microchannels.[55-67] Here, we show for the first time that the *location of chemically responsive groups* within flow-directed PNPs can determine the relative roles of size and internal structure in the resulting reaction kinetics. For junction linkages localized on PNP surfaces, the mean size is primarily important since the accessibility of linkages mean that reaction kinetics will depend on surface area alone and not on the internal PNP microstructure. On the other hand, for pendant linkages embedded within the PNP cores, the local environment and thus reactivity of linkages will depend on the specific molecular configuration of chains within the PNPs (described by G_{ex}). Similarly, our previous study of shear-directed photoresponsive PNPs, in which light-triggered reactive groups were embedded within the PNP core, also showed a strong correlation between reaction kinetics and PNP G_{ex},[60] supporting the current analysis.

CONCLUSIONS

In this work, we demonstrate microfluidic flow-directed self-assembly of biological stimuli-responsive block copolymers with cleavable linkages at dual-locations, namely the junction between hydrophilic and hydrophobic blocks and on pendant groups within the hydrophobic blocks. We show that self-assembly within a two-phase microfluidic reactor forms various "DualM" polymer nanoparticles (PNPs), including cylinders and multi-compartment vesicles, with sizes, morphologies, and complex inner compartment structures that are tunable with manufacturing flow rate. Microfluidic manufacturing leads to numerous kinetically-trapped intermediates between shear-dependent states, providing the most detailed mechanism to date of microfluidic PNP formation in the presence of flow-variable high shear. Moreover, glutathione (GSH)-triggered changes in PNP size and internal structure are found to depend strongly on the manufacturing method and flow rate as well as the location of linkages within the PNPs. Upon incubation in GSH, flow-directed PNPs with smaller mean sizes showed faster size increase, attributed to junction cleavage, and those with higher excess Gibbs free energy (lower thermodynamic stability) showed faster inner compartment growth, attributed to pendant cleavage.

These results suggest that by combining chemical synthetic control of functional group location and microfluidic shear control of PNP size and microstructure, finely-tuned biological responsivities can be achieved for specific nanomedicine applications.

ASSOCIATED CONTENT

Supporting Information

GPC and ^{1}H NMR characterization of the copolymer; Plot of cwc determination; Sample image for microfluidic two-phase gas-liquid flow; Table of actual flow conditions; Work flow of PNP RA_{compart} determination; RA_{compart} and N_{compart} plotted vs. microfluidic flow rate; Stability test of quenched DualM PNPs by TEM and DLS and resulting tabulated data; Additional TEM images showing evolution of LVs from discrete spherical to discrete cylindrical to highly interconnected cylindrical compartments; Plot of R_{RA} vs. $d_{\mathrm{h,eff,i.}}$

AUTHOR INFORMATION

Corresponding Author

* E-mail: mmoffitt@uvic.ca.

Notes

The authors declare no competing financial interest.

ACKNOWLEDGMENT

We are grateful to the Natural Sciences and Engineering Research Council of Canada, NSERC, for financial support. We also acknowledge Dr. Patrick Nahirney and Brent Gowen in the UVic EM lab (Department of Biology) for the continued use of their TEM.

REFERENCES

1. Allen, C.; Maysinger, D.; Eisenberg, A. Nano-Engineering Block Copolymer Aggregates for Drug Delivery. *Colloids Surf. B* **1999**, *16*, 3-27.

2. Maeda, H.; Wu, J.; Sawa, T.; Matsumura, Y.; Hori, K. Tumor Vascular Permeability and the EPR Effect in Macromolecular Therapeutics: A Review. *J. Controlled Release* **2000,** *65*, 271-284.

3. Kataoka, K.; Harada, A.; Nagasaki, Y. Block Copolymer Micelles for Drug Delivery: Design, Characterization and Biological Significance. *Adv. Drug Delivery Rev.* **2001,** *47*, 113-131.

4. Duncan, R. The Dawning Era of Polymer Therapeutics. *Nat. Rev. Drug Discov.* **2003,** *2,* 347-360.

5. Moghimi, S. M.; Hunter, A. C.; Murray, J. C. Nanomedicine: Current Status and Future Prospects. *Faseb J.* **2005,** *19*, 311-330.

6. Owens, D. E.; Peppas, N. A. Opsonization, Biodistribution, and Pharmacokinetics of Polymeric Nanoparticles. *Int. J. Pharm.* **2006,** *307*, 93-102.

7. Davis, M. E.; Chen, Z.; Shin, D. M. Nanoparticle Therapeutics: An Emerging Treatment Modality for Cancer. *Nat. Rev. Drug Discov.* **2008,** *7*, 771-782.

8. Alexis, F.; Pridgen, E.; Molnar, L. K.; Farokhzad, O. C. Factors Affecting the Clearance and Biodistribution of Polymeric Nanoparticles. *Mol. Pharmaceutics* **2008,** *5*, 505-515.

9. Kamaly, N.; Xiao, Z. Y.; Valencia, P. M.; Radovic-Moreno, A. F.; Farokhzad, O. C. Targeted Polymeric Therapeutic Nanoparticles: Design, Development and Clinical Translation. *Chem. Soc. Rev.* **2012,** *41*, 2971-3010.

10. Parveen, S.; Misra, R.; Sahoo, S. K. Nanoparticles: A Boon to Drug Delivery, Therapeutics, Diagnostics and Imaging. *Nanomed.: NBM* **2012,** *8*, 147-166.

11. Zhang, Y.; Chan, H. F.; Leong, K. W. Advanced Materials and Processing for Drug Delivery: The Past and the Future. *Adv. Drug Delivery Rev.* **2013,** *65*, 104-120.

12. Maeda, H.; Nakamura, H.; Fang, J. The EPR Effect for Macromolecular Drug Delivery to Solid Tumors: Improvement of Tumor Uptake, Lowering of Systemic Toxicity, and Distinct Tumor Imaging In Vivo. *Adv. Drug Delivery Rev.* **2013,** *65*, 71-79.

13. Bjornmalm, M.; Thurecht, K. J.; Michael, M.; Scott, A. M.; Caruso, F. Bridging Bio-Nano Science and Cancer Nanomedicine. *ACS Nano* **2017,** *11*, 9594-9613.

14. Chen, B. L.; Dai, W. B.; He, B.; Zhang, H.; Wang, X. Q.; Wang, Y. G.; Zhang, Q. Current Multistage Drug Delivery Systems Based on the Tumor Microenvironment. *Theranostics* **2017,** *7*, 538-558.

15. Perry, J. L.; Reuter, K. G.; Luft, J. C.; Pecot, C. V.; Zamboni, W.; DeSimone, J. M. Mediating Passive Tumor Accumulation through Particle Size, Tumor Type, and Location. *Nano Lett.* **2017,** *17*, 2879-2886.

16. Aftab, S.; Shah, A.; Nadhman, A.; Kurbanoglu, S.; Ozkan, S. A.; Dionysiou, D. D.; Shukla, S. S.; Aminabhavi, T. M. Nanomedicine: An Effective Tool in Cancer Therapy. *Int. J. Pharm.* **2018,** *540*, 132-149.

17. Brigger, I.; Dubernet, C.; Couvreur, P. Nanoparticles in Cancer Therapy and Diagnosis. *Adv. Drug Delivery Rev.* **2002,** *54*, 631-651.

18. Ferrari, M. Cancer Nanotechnology: Opportunities and Challenges. *Nat. Rev. Cancer* **2005,** *5*, 161-171.

19. Peer, D.; Karp, J. M.; Hong, S.; FaroKhzad, O. C.; Margalit, R.; Langer, R. Nanocarriers as An Emerging Platform for Cancer Therapy. *Nat. Nanotechnol.* **2007,** *2*, 751-760.

20. Liu, F.; Kozlovskaya, V.; Medipelli, S.; Xue, B.; Ahmad, F.; Saeed, M.; Cropek, D.; Kharlampieva, E. Temperature-Sensitive Polymersomes for Controlled Delivery of Anticancer Drugs. *Chem. Mater.* **2015,** *27*, 7945-7956.

21. Xiao, C. S.; Ding, J. X.; Ma, L. L.; Yang, C. G.; Zhuang, X. L.; Chen, X. S. Synthesis of Thermal and Oxidation Dual Responsive Polymers for Reactive Oxygen Species (ROS)-Triggered Drug Release. *Polym. Chem.* **2015,** *6*, 738-747.

22. Zou, H.; Yuan, W. Z. Temperature- and Redox-Responsive Magnetic Complex Micelles for Controlled Drug Release. *J. Mater. Chem. B* **2015,** *3*, 260-269.

23. Sharker, S. M.; Lee, J. E.; Kim, S. H.; Jeong, J. H.; In, I.; Lee, H.; Park, S. Y. pH Triggered In Vivo Photothermal Therapy and Fluorescence Nanoplatform of Cancer Based on Responsive Polymer-Indocyanine Green Integrated Reduced Graphene Oxide. *Biomaterials* **2015,** *61*, 229-238.

24. Gai, S. L.; Yang, G. X.; Yang, P. P.; He, F.; Lin, J.; Jin, D. Y.; Xing, B. G. Recent Advances in Functional Nanomaterials for Light-Triggered Cancer Therapy. *Nano Today* **2018,** *19*, 146-187.

25. Vankayala, R.; Hwang, K. C. Near-Infrared-Light-Activatable Nanomaterial-Mediated Phototheranostic Nanomedicines: An Emerging Paradigm for Cancer Treatment. *Adv. Mater.* **2018,** *30*, DOI: 10.1002/adma.201706320.

26. Zhang, L. L.; Wang, Y. Q.; Wang, J.; Wang, Y. L.; Chen, A. Y.; Wang, C.; Mo, W. T.; Li, Y. X.; Yuan, Q.; Zhang, Y. F. Photon-Responsive Antibacterial Nanoplatform for Synergistic Photothermal-/Pharmaco-Therapy of Skin Infection. *ACS Appl. Mater. Interfaces* **2019,** *11*, 300-310.

27. Chen, W.; Zhong, P.; Meng, F. H.; Cheng, R.; Deng, C.; Feijen, J.; Zhong, Z. Y. Redox and pH-Responsive Degradable Micelles for Dually Activated Intracellular Anticancer Drug Release. *J. Controlled Release* **2013,** *169*, 171-179.

28. Wen, Y. F.; Oh, J. K. Dual-Stimuli Reduction and Acidic pH-Responsive Bionanogels: Intracellular Delivery Nanocarriers with Enhanced Release. *RSC Adv.* **2014,** *4*, 229-237.

29. Hu, X. Y.; Wei, W.; Qi, X. L.; Yu, H.; Feng, L. D.; Li, J. J.; Wang, S. M.; Zhang, J. F.; Dong, W. Preparation and Characterization of a Novel pH-Sensitive Salecan-g-Poly(Acrylic Acid) Hydrogel for Controlled Release of Doxorubicin. *J. Mater. Chem. B* **2015,** *3*, 2685-2697.

30. Ellis, E.; Zhang, K. Y.; Lin, Q. Y.; Ye, E. Y.; Poma, A.; Battaglia, G.; Loh, X. J.; Lee, T. C. Biocompatible pH-Responsive Nanoparticles with a Core-Anchored Multilayer Shell of Triblock Copolymers for Enhanced Cancer Therapy. *J. Mater. Chem. B* **2017,** *5*, 4421-4425.

31. Guan, X. W.; Guo, Z. P.; Wang, T. H.; Lin, L.; Chen, J.; Tian, H. Y.; Chen, X. S. A pH-Responsive Detachable PEG Shielding Strategy for Gene Delivery System in Cancer Therapy. *Biomacromolecules* **2017,** *18*, 1342-1349.

32. Xu, X. F.; Pan, C. Y.; Zhang, W. J.; Hong, C. Y. Polymerization-Induced Self-Assembly Generating Vesicles with Adjustable pH-Responsive Release Performance. *Macromolecules* **2019,** *52*, 1965-1975.

33. Bajpai, A. K.; Shukla, S. K.; Bhanu, S.; Kankane, S. Responsive Polymers in Controlled Drug Delivery. *Prog. in Polym. Sci.* **2008,** *33*, 1088-1118.

34. Mura, S.; Nicolas, J.; Couvreur, P. Stimuli-Responsive Nanocarriers for Drug Delivery. *Nat. Mater.* **2013,** *12*, 991-1003.

35. Ganta, S.; Devalapally, H.; Shahiwala, A.; Amiji, M. A Review of Stimuli-Responsive Nanocarriers for Drug and Gene Delivery. *J. Controlled Release* **2008,** *126*, 187-204.

36. Cheng, R.; Feng, F.; Meng, F. H.; Deng, C.; Feijen, J.; Zhong, Z. Y. Glutathione-Responsive Nano-Vehicles as a Promising Platform for Targeted Intracellular Drug and Gene Delivery. *J. Controlled Release* **2011,** *152*, 2-12.

37. Oh, J. K. Disassembly and Tumor-Targeting Drug Delivery of Reduction-Responsive Degradable Block Copolymer Nanoassemblies. *Polym. Chem.* **2019,** *10*, 1554-1568.

38. Saito, G.; Swanson, J. A.; Lee, K. D. Drug Delivery Strategy Utilizing Conjugation via Reversible Disulfide Linkages: Role and Site of Cellular Reducing Activities. *Adv. Drug Delivery Rev.* **2003,** *55*, 199-215.

39. Russo, A.; Degraff, W.; Friedman, N.; Mitchell, J. B. Selective Modulation of Glutathione Levels in Human Normal Versus Tumor Cells and Subsequent Differential Response to Chemotherapy Drugs. *Cancer Res.* **1986**, *46*, 2845-2848.

40. Klaikherd, A.; Nagamani, C.; Thayumanavan, S. Multi-Stimuli Sensitive Amphiphilic Block Copolymer Assemblies. *J. Am. Chem. Soc.* **2009,** *131*, 4830-4838.

41. Tang, L. Y.; Wang, Y. C.; Li, Y.; Du, J. Z.; Wang, J. Shell-Detachable Micelles Based on Disulfide-Linked Block Copolymer as Potential Carrier for Intracellular Drug Delivery. *Bioconjug. Chem.* **2009,** *20*, 1095-1099.

42. Liu, J. Y.; Huang, W.; Pang, Y.; Zhu, X. Y.; Zhou, Y. F.; Yan, D. Y. Hyperbranched Polyphosphates for Drug Delivery Application: Design, Synthesis, and In Vitro Evaluation. *Biomacromolecules* **2010,** *11*, 1564-1570.

43. Chen, W.; Yang, H. C.; Wang, R.; Cheng, R.; Meng, F. H.; Wei, W. X.; Zhong, Z. Y. Versatile Synthesis of Functional Biodegradable Polymers by Combining Ring-Opening Polymerization and Postpolymerization Modification via Michael-Type Addition Reaction. *Macromolecules* **2010,** *43*, 201-207.

44. Cai, X. J.; Dong, H. Q.; Xia, W. J.; Wen, H. Y.; Li, X. Q.; Yu, J. H.; Li, Y. Y.; Shi, D. L. Glutathione-Mediated Shedding of PEG Layers Based on Disulfide-Linked Catiomers for DNA Delivery. *J. Mater. Chem.* **2011,** *21*, 14639-14645.

45. Sourkohi, B. K.; Cunningham, A.; Zhang, Q.; Oh, J. K. Biodegradable Block Copolymer Micelles with Thiol-Responsive Sheddable Coronas. *Biomacromolecules* **2011,** *12*, 3819-3825.

46. Zhang, Q.; Ko, N. R.; Oh, J. K. Recent Advances in Stimuli-Responsive Degradable Block Copolymer Micelles: Synthesis and Controlled Drug Delivery Applications. *Chem. Commun.* **2012,** *48*, 7542-7552.

47. Zhang, Q.; Ko, N. R.; Oh, J. K. Modulated Morphologies and Tunable Thiol-Responsive Shedding of Aqueous Block Copolymer Aggregates. *RSC Adv.* **2012,** *2*, 8079-8086.

48. Khorsand, B.; Lapointe, G.; Brett, C.; Oh, J. K. Intracellular Drug Delivery Nanocarriers of Glutathione-Responsive Degradable Block Copolymers Having Pendant Disulfide Linkages. *Biomacromolecules* **2013,** *14*, 2103-2111.

49. Cunningham, A.; Oh, J. K. New Design of Thiol-Responsive Degradable Polylactide-Based Block Copolymer Micelles. *Macromol. Rapid Commun.* **2013,** *34*, 163-168.

50. Chan, N.; Khorsand, B.; Aleksanian, S.; Oh, J. K. A Dual Location Stimuli-Responsive Degradation Strategy of Block Copolymer Nanocarriers for Accelerated Release. *Chem. Commun.* **2013,** *49*, 7534-7536.

51. Wan, Y. M.; Bu, Y.; Liu, J. M.; Yang, J.; Cai, W. Q.; Yin, Y. H.; Xu, W. J.; Xu, P. H.; Zhang, J. L.; He, M. pH and Reduction-Activated Polymeric Prodrug Nanoparticles Based on a 6-Thioguanine-Dialdehyde Sodium Alginate Conjugate for Enhanced Intracellular Drug Release in Leukemia. *Polym. Chem.* **2018,** *9*, 3415-3424.

52. Karnik, R.; Gu, F.; Basto, P.; Cannizzaro, C.; Dean, L.; Kyei-Manu, W.; Langer, R.; Farokhzad, O. C. Microfluidic Platform for Controlled Synthesis of Polymeric Nanoparticles. *Nano Lett.* **2008,** *8*, 2906-2912.

53. Xu, Q. B.; Hashimoto, M.; Dang, T. T.; Hoare, T.; Kohane, D. S.; Whitesides, G. M.; Langer, R.; Anderson, D. G. Preparation of Monodisperse Biodegradable Polymer Microparticles Using a Mcrofluidic Flow-Focusing Device for Controlled Drug Delivery. *Small* **2009,** *5*, 1575-1581.

54. Capretto, L.; Carugo, D.; Mazzitelli, S.; Nastruzzi, C.; Zhang, X. L. Microfluidic and Lab-on-a-Chip Preparation Routes for Organic Nanoparticles and Vesicular Systems for Nanomedicine Applications. *Adv. Drug Delivery Rev.* **2013,** *65*, 1496-1532.

55. Wang, C. W.; Sinton, D.; Moffitt, M. G. Flow-Directed Block Copolymer Micelle Morphologies via Microfluidic Self-Assembly. *J. Am. Chem. Soc.* **2011,** *133*, 18853-18864.

56. Wang, C. W.; Bains, A.; Sinton, D.; Moffitt, M. G. Flow-Directed Assembly of Block Copolymer Vesicles in the Lab-on-a-Chip. *Langmuir* **2012,** *28*, 15756-15761.

57. Wang, C. W.; Bains, A.; Sinton, D.; Moffitt, M. G. Flow-Directed Loading of Block Copolymer Micelles with Hydrophobic Probes in a Gas-Liquid Microreactor. *Langmuir* **2013,** *29*, 8385-8394.

58. Wang, C. W.; Sinton, D.; Moffitt, M. G. Morphological Control via Chemical and Shear Forces in Block Copolymer Self-Assembly in the Lab-on-Chip. *ACS Nano* **2013,** *7*, 1424-1436.

59. Bains, A.; Cao, Y. M.; Moffitt, M. G. Multiscale Control of Hierarchical Structure in Crystalline Block Copolymer Nanoparticles Using Microfluidics. *Macromol. Rapid. Commun.* **2015,** *36*, 2000-2005.

60. Xu, Z. Q.; Yan, B.; Riordon, J.; Zhao, Y.; Sinton, D.; Moffitt, M. G. Microfluidic Synthesis of Photoresponsive Spool-Like Block Copolymer Nanoparticles: Flow-Directed Formation and Light-Triggered Dissociation. *Chem. Mater.* **2015,** *27*, 8094-8104.

61. Xu, Z. Q.; Lu, C. H.; Riordon, J.; Sinton, D.; Moffitt, M. G. Microfluidic Manufacturing of Polymeric Nanoparticles: Comparing Flow Control of Multiscale Structure in Single-Phase Staggered Herringbone and Two-Phase Reactors. *Langmuir* **2016,** *32*, 12781-12789.

62. Bains, A.; Wulff, J. E.; Moffitt, M. G. Microfluidic Synthesis of Dye-Loaded Polycaprolactone-Block-Poly(Ethylene Oxide) Nanoparticles: Insights into Flow-Directed Loading and In Vitro Release for Drug Delivery. *J. Colloid Interface Sci.* **2016,** *475*, 136-148.

63. Bains, A.; Cao, Y. M.; Kly, S.; Wulff, J. E.; Moffitt, M. G., Controlling Structure and Function of Polymeric Drug Delivery Nanoparticles Using Microfluidics. *Mol. Pharmaceutics* **2017,** *14*, 2595-2606.

64. Bains, A.; Moffitt, M. G. Effects of Chemical and Processing Variables on Paclitaxel-Loaded Polymer Nanoparticles Prepared Using Microfluidics. *J. Colloid Interface Sci.* **2017,** *508*, 203-213.

65. Xu, Z. Q.; Lu, C. H.; Lindenberger, C.; Cao, Y. M.; Wulff, J. E.; Moffitt, M. G. Synthesis, Self-assembly, and Drug Delivery Characteristics of Poly(Methyl Caprolactone-co-Caprolactone)-b-Poly(Ethylene Oxide) Copolymers with Variable Compositions of Hydrophobic Blocks: Combining Chemistry and Microfluidic Processing for Polymeric Nanomedicines. *ACS Omega* **2017,** *2*, 5289-5303.

66. Chen, R. Y.; Wulff, J. E.; Moffitt, M. G. Microfluidic Processing Approach to Controlling Drug Delivery Properties of Curcumin-Loaded Block Copolymer Nanoparticles. *Mol. Pharmaceutics* **2018,** *15*, 4517-4528.

67. Cao, Y. M.; Silverman, L.; Lu, C. H.; Hof, R.; Wulff, J. E.; Moffitt, M. G. Microfluidic Manufacturing of SN-38-Loaded Polymer Nanoparticles with Shear Processing Control of Drug Delivery Properties. *Mol. Pharmaceutics* **2019,** *16*, 96-107.

68. Britovsek, G. J. P.; England, J.; White, A. J. P. Non-heme Iron(II) Complexes Containing Tripodal Tetradentate Nitrogen Ligands and Their Application in Alkane Oxidation Catalysis. *Inorg. Chem.* **2005,** *44*, 8125-8134.

69. Zhang, Q.; Aleksanian, S.; Nohbc, S. M.; Oh, J. K. Thiol-Responsive Block Copolymer Nanocarriers Exhibiting Tunable Release with Morphology Changes. *Polym. Chem.* **2013,** *4*, 351-359.

70. Jiang, X. Q.; Yu, Y.; Chen, J. W.; Zhao, M. K.; Chen, H.; Song, X. Z.; Matzuk, A. J.; Carroll, S. L.; Tan, X.; Sizovs, A.; Cheng, N. H.; Wang, M. C.; Wang, J. Quantitative Imaging of Glutathione in Live Cells Using a Reversible Reaction-Based Ratiometric Fluorescent Probe. *ACS Chem. Biol.* **2015**, *10*, 864-874.

71. Jain, S.; Bates, F. S. On the Origins of Morphological Complexity in Block Copolymer Surfactants. *Science* **2003,** *300*, 460-464.

TOC Figure

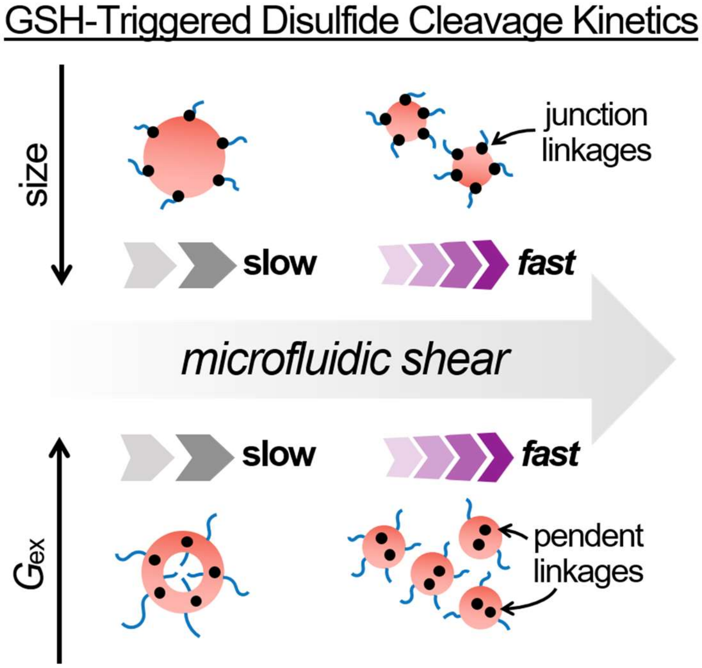
GSH-Triggered Disulfide Cleavage Kinetics
size
junction linkages
slow
fast
microfluidic shear
slow
fast
G_{ex}
pendent linkages